Master's thesis

NTNU
Norwegian University of Science and Technology
Faculty of Natural Sciences
Department of Physics

Birk Engegård

Extracting OH airglow intensity from the background of the Nordic Optical Telescope

Master's thesis in Applied Physics and Mathematics
Supervisor: Patrick Joseph Espy
June 2019

NTNU
Norwegian University of
Science and Technology

Birk Engegård

Extracting OH airglow intensity from the background of the Nordic Optical Telescope

Master's thesis in Applied Physics and Mathematics
Supervisor: Patrick Joseph Espy
June 2019

Norwegian University of Science and Technology
Faculty of Natural Sciences
Department of Physics

NTNU
Norwegian University of
Science and Technology

I do not correct my mistakes,
my mistakes correct me.
Solely through failure
may I achieve perfection.

This work is the culmination of a quarter-century of failures and mistakes.

Preface

This thesis, written during the spring semester of 2019, is the final work carried out in order to complete a Master of Science degree in applied physics and mathematics at the Norwegian University of Science and Technology (NTNU). It is the continuation of the specialization project titled "*Assessment of background data from the Nordic Optical Telescope for long-term airglow studies*" written during the autumn semester of 2018.

Special thanks to my supervisor, Dr. Patrick Espy, for patiently dissecting my ramblings along the way and for offering your own ramblings in return. Together we conquered the devil in the details. I would also like to thank soon-to-be Dr. Christoph Franzen for unprecedented and vital guidance related to the implementation of the data processing, and good company during supervision of the next generation in the physics lab.

Many thanks to Stava for being an exemplary flat mate all these years. Your culinary expertise, great taste in multimedia entertainment and exquisite companionship has made the pursuance of higher education a memorable and rejoiceful experience.

I would also like to express sincere gratitude and appreciation to my excellent colleagues at ENT3R Realfagstrening, and to the friendly and sporty community in NTNUI Tennis and Trondhjems Tennisklubb. Shout-outs as well to Odd-Einar and Markus, whose company I could always count on at "Fysikkland" during the many late nights of writing.

Finally, I want to thank everyone who ever taught me anything and inspired me, all the wonderful people I have met along the way, who broadened my horizon, my friends and family, and of course the welfare state of Norway for giving me the opportunity to take on the endeavours of pursuing a higher education.

Abstract

Airglow emitted from the OH radical in the middle atmosphere is a strong source of near-infrared radiation. Although the radiance is an inconvenient and unavoidable source of background noise in ground-based near-infrared astronomy, the spectral properties of the airglow can also provide valuable information about the conditions and dynamics of the middle atmosphere.

The goal of this thesis is to study the intensity of the airglow. This is done by developing an algorithm capable of extracting the $(3, 1)$, $(4, 2)$, $(5, 3)$, $(6, 4)$ and $(9, 7)$ transition Q-branches of the airglow from the background noise present in the archived data of the Nordic Optical Telescope (NOT), La Palma, Spain. Subsequently, the nighttime cycle of the airglow intensity was analyzed in terms of local solar time (LST) and hours past sunset, and the seasonal cycle was studied using monthly means. Furthermore, the seasonal cycle obtained using the NOT was compared with satellite data from the Sounding of the Atmosphere using Broadband Emmision Radiometry (SABER) instrument mounted on the Thermosphere-Ionosphere-Mesosphere Energetics and Dynamics (TIMED) satellite.

As the distribution of the available observations was scattered and sparse within each year, archived data from 2008 to 2016 was combined to study the nighttime and seasonal cycle. Trends exceeding a year, such as effects driven by the solar cycle, can thus distort the results to some degree. However, it was concluded that the results are valid indications of the nighttime and seasonal trends. Agreement between the seasonal cycle obtained by NOT and SABER supports this claim.

For the nighttime trend, a semi-diurnal cycle was found, with an intensity decrease after sunset, a minimum between 19 and 21 local solar time, a maximum between 21 and 22 LST, a new minimum at 01-02 LST before an intensity rise towards dawn. The seasonal trend showed a semi-annual cycle, with intensities decreasing from January to February, a rise towards May, a minimum in June before an intensity rise towards November. No data was available for December. SABER data agrees with the rise from February to May, but has a slower decrease and rise in the proceeding months. The high intensities in November and January are not present in the SABER data. Nevertheless, the SABER data was collected using a zonal mean. Therefore, the apparent discrepancies could be caused by local effects at the geographical location of the NOT.

Sammendrag

Nattehimmellys fra OH-radikalet i mellomatmosfæren er en sterk kilde til nær infrarød stråling. Til tross for at strålingen er en besværlig og uunngåelig kilde til bakgrunnsstøy i bakkebasert nær infrarød astronomi, kan de spektrale egenskapene til nattehimmellyset gi verdifull informasjon om forholdene og dynamikken i mellomatmosfæren.

Hensikten med denne oppgaven er å studere intensiteten av nattehimmellyset. Dette er gjort ved å utvikle en algoritme som er i stand til å trekke ut intensiteten av $(3, 1)$, $(4, 2)$, $(5, 3)$, $(6, 4)$ og $(9, 7)$ overgangenes Q-forgreninger av nattehimmellyset fra bakgrunnstøyen i arkivert data fra "the Nordic Optical Telescope" (NOT), La Palma, Spania. Deretter ble den nattlige intensitetsyklsen analysert som funksjon av lokal soltid (LST) og timer etter solnedgang, og den årlige syklysen ble studert ved å bruke månedlige intensitetsgjennomsnitt. I tillegg til dette ble den årlige syklusen sammenlignet med data fra "Sounding of the Atmosphere using Broadband Emmision Radiometry" (SABER), som er et instrument montert på satelitten "Thermosphere-Ionosphere-Mesosphere Energetics and Dynamics" (TIMED).

Siden fordelingen av tilgjengelige observasjoner var tynnspredt innenfor hvert enkelt år, ble arkivert data fra 2008 til 2016 slått sammen for å studere både den nattlige og årlige syklusen. Sykluser som går over flere år, som for eksempel solsyklusen, kan dermed fordreie resultatene til en viss grad. Det ble likevel konkludert med at resultatene gir en gyldig indikasjon av den nattlige og årlige syklusen. Overenstemmelse mellom den årlige syklusen funnet av NOT og SABER styrker påstanden.

For den nattlige syklusen, ble en semi-nattlig syklus funnet, med en intensitetsnedgang etter solnedgang, et minimum mellom 19 og 21 LST, et maksimum mellom 21 og 22 LST, et nytt minimum mellom 01 og 02 LST, før en intensitetsøkning mot soloppgang. Den årlige syklusen viste en semi-årlig syklus, med en intensitetsnedgang fra januar til februar, en økning mot mai, et minimum i juni før en økning mot november. Ingen data var tilgjengelig for desember. Dataene fra SABER stemmer overens med økningen fra februar til mai, men har en slakere nedgang og økning i de følgende månedene. De høye intensitene i november og januar er ikke til stede i dataene fra SABER. Likevel, dataene fra SABER er hentet fra et sonalt gjennomsnitt. Dermed kan de tilsynelatende uoverstemmelsene stamme fra lokale effekter ved NOT sin geografiske plassering.

Table of Contents

List of Tables

List of Figures

Abbreviations

ADU	=	Analog-to-Digital Unit
a.u.	=	Arbitrary Units
FITS	=	Flexible Image Transport System
netCDF	=	Network Common Data Form
HgCdTe	=	Mercury Cadmium Telluride
IPCC	=	Intergovernmental Panel on Climate Change
M	=	Mediator (any species in the atmosphere)
MLT	=	Mesophere & Lower Thermosphere
NOT	=	Nordic Optical Telescope
NOTCam	=	Nordic Optical Telescope near-infrared Camera and spectrograph
MAD	=	Mean Absolute Deviation
RMSD	=	Root-Mean-Square Deviation
LST	=	Local Solar Time
TIMED	=	Thermosphere-Ionosphere-Mesosphere Energetics and Dynamics
SABER	=	Sounding of the Atmosphere using Broadband Emmision Radiometry
PDFAM	=	Percentage Deviation From Annual Mean
IPCC	=	Intergovernmental Panel on Climate Change
UTC	=	Coordinated Universal Time

Chapter 1

Introduction

The impact of anthropogenic climate change and global warming have been hot topics in scientific communities worldwide. To accurately predict the long- and short-term climate trends the Intergovernmental Panel on Climate Change (IPCC) relies on climate models simulating a vast amount of atmospheric processes [1]. These models improve with increased knowledge of the physics and chemistry behind each process, how they are interconnected in dynamical systems, and how they behave in different regions and atmospheric layers. One region of interest is the mesosphere and lower thermosphere, or MLT region. An interesting phenomenon present there is the airglow radiated by the hydroxyl radical OH. The OH airglow emits characteristic spectral lines in the near-infrared part of the electromagnetic spectrum [2, 3] and studying how strong these lines are relative to each other and how they vary with respect to time and location on the sky can give a great deal of information about the climatology and dynamics of the MLT region. Measurements of the OH intensity can be used to infer the concentrations of the highly reactive and abundant atomic oxygen O in the MLT [4], and if the ozone O_3 concentrations are known, atomic hydrogen H and chemical heating rates can also be inferred [5, 6]. The measured intensities can also be used to derive the radiative energy loss of the emitting OH, and the momentum deposition of gravity waves [7, 8]. The energy budget of the MLT region, which is of utmost importance for climate models, is thus intimately linked to the airglow intensity. Hydroxyl airglow is also linked to the nocturnal $4.3\,\mu\mathrm{m}$ emission line from CO_2, and important in the research carried out in order to understand the mechanisms contributing to the emission [9, 10, 11]. Additionally, attempts at modelling the airglow intensity have not conformed with observations [12], which calls for more research on the topic. Consequently, it is clear that documenting measurements of the airglow and improving experimental techniques to increase the availability of data and locations is important in order to compare theoretical prediction with experimental observation and of great interest to the scientific community.

Airglow is also a dominating source of noise for ground-based spectrography observatories looking at astronomical objects in the near-infrared, such as the Nordic Optical Telescope (NOT). Spectral lines from the OH layer will then be superimposed on the spec-

trum of the intended target as inevitable background noise. However, if the spectrum of the intended target is removed from the background noise structure, only the spectral lines of the airglow remains, which can be used for atmospheric studies. The goal of this thesis is to advance a method of extracting those OH lines from the spectra acquired by the Nordic Optical Telescope near-infrared Camera and spectrograph (NOTCam) [13] and applying it to large amounts of archived data in the time frame from 2008 to 2016. This is done for the Q-branches of the $(3, 1)$, $(4, 2)$, $(5, 3)$, $(6, 4)$ transitions in the H band, and $(9, 7)$ transition in the K band. The acquired intensities will then be used to study the nighttime and seasonal intensity trends of the OH airglow layer, which is also beneficial to the NOT astronomers when planning observations of faint astronomical objects. Finally, the seasonal cycle is compared with data gathered from the Sounding of the Atmosphere using Broadband Emmision Radiometry (SABER) instrument mounted on the Thermosphere-Ionosphere-Mesosphere Energetics and Dynamics (TIMED) satellite.

This thesis will begin with describing a few basic properties of the atmosphere and OH airglow in Chapter 2, before giving an instrumental overview of the NOTCam in Chapter 3. A short description of the SABER instrument and TIMED satellite is also given there. Chapter 4 outlines the implementational procedures and data processing techniques used for both the NOTCam and SABER data, before the results are presented in Chapter 5. Finally, an outlook on further research and implications is given in Chapter 6 before the thesis is concluded in Chapter 7.

The work presented here is the continuation of the author's specialization project [14], and some sections and results are previously presented there. Specifically, most of Chapter 2, the parts concerning NOTCam in Chapter 3 and Chapter 4, and the initial results regarding the flat fields and H band in Chapter 5.

Chapter 2

Theory

This chapter will cover the fundamental theory concerning the atmosphere and the OH airglow layer that the studies described in this thesis is built upon. Section 2.1 gives a description of the different atmospheric layers and outlines the properties of the surroundings of the OH layer. The main causes of variability in the middle atmosphere is mentioned in Section 2.2 and Section 2.3 describes the photochemical dynamics of the OH layer in greater detail and explains how the intensities and compositions of the layer can be studied using near-infrared spectroscopy.

2.1 Atmospheric structure

The atmosphere is a mixture of gases bound by Earth's gravity [15]. The gases interact with each other, the Sun's radiation and the surface of the Earth. The thermodynamic and photochemical properties of the atmospheric gases are dependent on their altitude. That is, the atmosphere can be divided into layers, where each layer is characterized by having similar interaction properties. By convention, the layers are defined by their temperature gradient [16].

The layer closest to the surface of the Earth is the troposphere. Here, the atmospheric temperature decreases with altitude until a local minimum is reached in the tropopause at around $15\,\mathrm{km}$ at equatorial latitudes. The height of the tropopause decreases with latitude towards the polar regions where it as at approximately $9\,\mathrm{km}$. The troposphere is characterized by convection, cloud formation, wind, and rain. In other words, it is where weather takes place. The troposphere is well-mixed due to high density, with heating rates caused primarily by the surface of the Earth heating the atmosphere above. Absorption of solar light by minor atmospheric species such as CO_2 also adds a small contribution to the heating rate.

Above the tropopause, the stratosphere extends to an altitude of about $50\,\mathrm{km}$. The stratosphere is characterized by a temperature that increases with altitude until a local maximum in the stratopause. The stratospheric heating is caused by the short-wave radiation from the sun interacting with ozone, which is abundant in this layer. This is why the

temperature increases with altitude, in contrast to the case in the troposphere.

The mesosphere is on top of the stratopause. Here, since there is little absorption, and cooling due to CO_2 [17], the temperature again drops with altitude. The temperature decreases until a minimum is reached in the mesopause, which coldest region of the atmosphere at an altitude of $80\,\mathrm{km}$ in the summer and $90\,\mathrm{km}$ in the winter. Even though the atmosphere remains well-mixed through the mesosphere, this region is characterized by very low pressure and density.

The uppermost layer is the thermosphere where temperature again rises with altitude due to absorption of extreme ultraviolet solar radiation by O_2 and N_2. The thermosphere extends outwards until the pressure and density drops off to a level where terrestrial particles can no longer be detected. The mesosphere and lower thermosphere (MLT) region is where the OH layer is situated at an average height of $88.4\,\mathrm{km}$ at middle latitudes [18]. A conceptual illustration of the atmosphere is given in Figure 2.1.

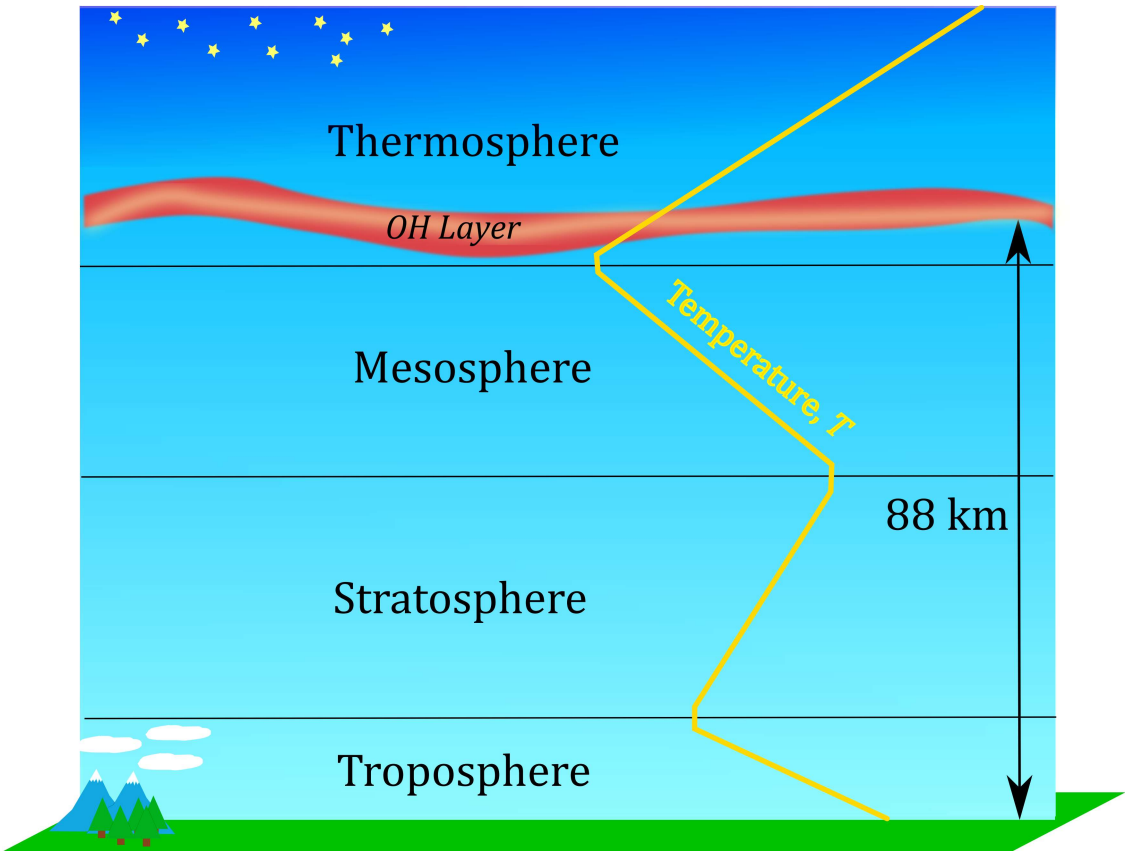

Figure 2.1: Conceptual illustration of how the atmosphere is divided into the troposphere, stratosphere, mesosphere, and thermosphere. The OH layer is also included in red to represent the infrared glow. The yellow line qualitatively shows the temperature as a function of altitude with increasing temperatures towards the right.

2.2 Dynamics of the MLT

The dynamics of the MLT region is dominated by atmospheric tides and gravity waves. Atmospheric tides are periodic variations in density, pressure and temperature that drives changes the composition of the MLT. The dominating atmospheric tides in the MLT have periods of 24 hours (diurnal) and 12 hours (semi-diurnal), but tides of other periods are also present. Tides can be either migrating or non-migrating. Migrating tides follow the motion of the sun around the globe, whereas non-migrating tides are aperiodic relative to the sun and can propagate westward and eastward. Migrating tides are driven by absorption of solar infrared radiation by water vapor in the troposphere and absorption of ultraviolet solar radiation by ozone in the stratosphere. Non-migrating tides are generated by local effects such as differences in tropospheric latent heat due to landmasses. Even though the tides are generated in the lower atmohsphere, they become significant in the MLT [19].

Gravity waves are upward propagating waves that deposit momentum and energy into the MLT region. A comprehensive review of gravity waves in the middle atmosphere can be found in [20]. Tides and waves change the composition of the MLT on short-term and long-term time scales. These composition changes will in turn cause variability in the OH layer. A review of how tides and waves affect the MLT region can be found in [21].

Photochemical effects also play an important role in the composition of the MLT. These effects are driven by photons interacting with atmospheric species. During day-time, photons interacting with atmospheric species such as O_2, O_3 and H_2O play a key role in the dynamics revolved around OH production [22, chapter 2]. At night, when photons are no longer introduced into the system, the reactions described in Section 2.3.1 takes over and new dynamical systems occur. Towards dawn, O and O_2 produced by sunlight from the east can be introduced into the system and cause drastic composition changes.

2.3 The OH layer

This section focuses on the OH layer. First, the photochemistry behind the airglow is detatiled, before a brief overview of the spectroscopy that is relevant for this thesis is given.

2.3.1 Photochemistry

The primary reaction responsible for the production of excited OH is given by

$$\mathrm{H} + \mathrm{O_3} \longrightarrow \mathrm{OH}(v, J) + \mathrm{O_2}, \tag{2.1}$$

where H and OH are commonly written as H^* and OH^* to specify that they are radicals, meaning they have an unpaired electron and are highly reactive [23], or that the molecules have some degree of internal excitation. Reaction (2.1) is exothermic leaving the OH radical in an excited state with vibration quantum number v and rotation quantum number J [24]. Here the J states form a fine-structure within each v state [16, Chapter 3]. Further in this report, whenever a state v is referred to, it is also implied that this state contains several J states. The production rate $P_{\mathrm{OH(v)}}$ of OH in a given v state from Reaction (2.1)

is given by

$$P_{\mathrm{OH}(v)} = k_{\mathrm{H+O_3}}(v)[\mathrm{H}][\mathrm{O_3}], \tag{2.2}$$

where $k_{\mathrm{H+O_3}}(v)$ the v dependent reaction rate of H + O_3 also accounting for the branching ratios of different v states. The brackets indicate concentrations or number densities.

There are several processes where the OH radical can react with other species in the MLT region. One is the quenching reaction with a mediator M,

$$\mathrm{OH}(v') + \mathrm{M} \longrightarrow \mathrm{OH}(v'') + \mathrm{M}, \tag{2.3}$$

where the OH molecule transitions from an initial upper state v' to a final lower state v'' by transferring energy to the mediator. It is debated whether Reaction (2.3) happens stepwise, that is $v'' = v' - 1$ or if it is a sudden death process where the vibration level goes directly to the lowest vibration state $v'' = 0$ [25]. The removal rate R_{M} of Reaction (2.3), which is equivalent to removal of $\mathrm{OH}(v')$ and production of $\mathrm{OH}(v'')$, is given by

$$R_{\mathrm{M}} = k_{\mathrm{OH}(v')+\mathrm{M}}[\mathrm{OH}(v')][\mathrm{M}], \tag{2.4}$$

where [M] is the air density in the MLT region. If the mediator M is oxygen O, another quenching reaction

$$\mathrm{OH}(v') + \mathrm{O} \longrightarrow \mathrm{O_2} + \mathrm{H} \tag{2.5}$$

is possible with reaction rate

$$R_{\mathrm{O}} = k_{\mathrm{OH}(v')+\mathrm{O}}[\mathrm{OH}(v')][\mathrm{O}], \tag{2.6}$$

where the OH radical is dissociated, thus deactivating the OH cycle.

The OH radical can also undergo transitions from higher vibration states v' to lower states v'' by emitting a photon γ,

$$\mathrm{OH}(v') \longrightarrow \mathrm{OH}(v'') + \gamma. \tag{2.7}$$

The reaction rate R_γ of Reaction (2.7) is given by

$$R_\gamma = A_{v'}^{v''}[\mathrm{OH}(v')], \tag{2.8}$$

where $A_{v'}^{v''}$ is the Einstein coefficient giving the probability of a transition $v' \longrightarrow v''$ occurring. The OH molecule is short-lived and therefore in photochemical equilibrium [12]. That is, the accumulated production of OH in state v, given by

$$P_{\mathrm{OH}(v)} + \sum_{v'>v} R_M(v' \longrightarrow v) + \sum_{v'>v} R_\gamma(v' \longrightarrow v), \tag{2.9}$$

equals the accumulated loss of OH from state v

$$\sum_{v>v''} R_M(v \longrightarrow v'') + \sum_{v>v''} R_\gamma(v \longrightarrow v''). \tag{2.10}$$

The concentration of OH in a given vibration state v can then be found by equating loss and production, factoring out $[\mathrm{OH}(v)]$ from the loss terms and dividing by the remaining factor. This yields

$$[\mathrm{OH}(v)] = \frac{P_{\mathrm{OH}(v)} + \sum\limits_{v'>v} k_{\mathrm{OH(v')+M}}[\mathrm{OH}(v')][\mathrm{M}] + \sum\limits_{v'>v} A^{v}_{v'>v}[\mathrm{OH}(v')]}{\sum\limits_{v>v''} A^{v''}_{v>v''} + \sum\limits_{v>v''} k_{\mathrm{OH}(v)+\mathrm{M}}[\mathrm{M}] + k_{\mathrm{OH}(v)+\mathrm{O}}[\mathrm{O}]}. \tag{2.11}$$

Additionally, at night time, the ozone in the MLT region is produced through

$$\mathrm{O} + \mathrm{O_2} + \mathrm{M} \longrightarrow \mathrm{O_3} + \mathrm{M} \tag{2.12}$$

and lost in Reaction (2.1). Equating production rate and loss rate the ozone concentration yields

$$[\mathrm{O_3}] = \frac{k_{\mathrm{O+O_2+M}}[\mathrm{O}][\mathrm{O_2}][\mathrm{M}]}{k_{\mathrm{H+O_3}}[\mathrm{H}]}. \tag{2.13}$$

Combining Equation (2.2) and Equation (2.13), Equation (2.11) can be re-written as

$$[\mathrm{OH}(v)] = \frac{k_{\mathrm{O+O_2+M}}[\mathrm{O}][\mathrm{O_2}][\mathrm{M}] + \sum\limits_{v'>v} k_{\mathrm{OH(v')+M}}[\mathrm{OH}(v')][\mathrm{M}] + \sum\limits_{v'>v} A^{v}_{v'>v}[\mathrm{OH}(v')]}{\sum\limits_{v>v''} A^{v''}_{v>v''} + \sum\limits_{v>v''} k_{\mathrm{OH}(v)+\mathrm{M}}[\mathrm{M}] + k_{\mathrm{OH}(v)+\mathrm{O}}[\mathrm{O}]}. \tag{2.14}$$

Equation (2.14) may seem cumbersome, but upon closer inspection it becomes clear that given comprehensive knowledge about the OH concentrations in different v states, the constants k's and A's, and air density M, the concentrations of O and $\mathrm{O_2}$ can be studied. For $\mathrm{OH}(9)$ in particular, the terms including v' in the numerator vanishes as Reaction (2.1) only produces v states up to $v = 9$. Furthermore, at such high vibration levels, the loss due to radiation is much higher than the loss due to quenching, and if these terms are neglected Equation (2.14) simplifies to

$$[\mathrm{OH}(9)] = \frac{k_{\mathrm{O+O_2+M}}[\mathrm{O}][\mathrm{O_2}][\mathrm{M}]}{\sum\limits_{v''=0}^{8} A^{v''}_{9}}, \tag{2.15}$$

which in a more condensed manner shows the connection between the OH radical and other key species in the MLT region. For example, Equation 2.15 can be used to deduce concentration of atomic oxygen O, which is an important and reactive species that is difficult to measure in the MLT region.

2.3.2 Spectroscopy

An analysis of the $\mathrm{OH}(v)$ states can be done by applying spectrometric techniques to the photon emitted in Reaction (2.7). Here, the reaction is rewritten slightly to specify the importance of the fine-structure from the J states:

$$\mathrm{OH}(v', J') \longrightarrow \mathrm{OH}(v'', J'') + \gamma. \tag{2.16}$$

The photon γ will appear at a wavelength λ given by

$$\lambda = \frac{hc}{\Delta E}, \tag{2.17}$$

where h is Planck's constant, c is the speed of light and ΔE is the energy difference between an initial upper state (v', J') and a lower final state (v'', J''). Note that in spectroscopy, whenever a difference Δ is mentioned it is implied that the low energy state is subtracted from the high energy state [26]. The photons form an emission spectrum with spectral lines at wavelengths λ corresponding to a certain vibration-rotation transition and intensity proportional to how frequently the transition occurs.

For the OH molecule, $\Delta J = J' - J''$ follow selection rules $\Delta J = \pm 1$ or $\Delta J = 0$. In spectroscopy, spectral lines originating from a transition $v' \longrightarrow v''$ with $\Delta J = -1$ is referred to as the P-branch, $\Delta J = +1$ as the R-branch and $\Delta J = 0$ as the Q-branch [27]. For a given vibration transition (v', v''), all the possible ΔJ's will form a set of spectral lines referred to as the (v', v'') band.

Spectral lines are labeled according to their branch and final rotation number $N'' = J'' + s$ where s is spin originating from electron configuration. The OH radical exists in two states F_1 and F_2 with different electron configurations. In state F_1, the J levels are given by $3/2 + n$ where n is an integer, and $s = -1/2$. Similarly for F_2, $J = 1/2 + n$ with $s = 1/2$. A sub-script is used to indicate which state a transition is from. For example, $R_1(2)$ is a spectral line in the R-branch and $N'' = 2$ from the F_1 state. For the Q-branch, lines from state F_1 and F_2 will be on top of each other, and the subscript is therefore omitted. An illustration of the vibration-rotation states and transitions is given in Figure 2.2 and an example of a rotation-vibration band, with labeled spectral lines, is given in Figure 2.3.

The intensity $I_{v',J'}^{v'',J''}$ of a spectral line originating from a transiting between initial state (v', J') and final state (v'', J'') is given by

$$I_{v',J'}^{v'',J''} = N_{v',J'} A_{v',J'}^{v'',J''}, \tag{2.18}$$

where $N_{v',J'}$ is the number density of OH in the initial state and $A_{v',J'}^{v'',J''}$ is the Einstein emission coefficient of the transition in emissions per second. Thus, it is possible to determine the OH concentration in a given state by measuring the line intensity, since the Einstein coefficients are known [28, 29].

Since the rotation level energies are closely spaced, collisions are effective at distributing the rotation manifold within the OH radical into a Boltzmann distribution. Thus, the relative intensities of the transitions within a (v', v'') band are dependent on temperature, however the total intensity of each branch is temperature independent [30, Page 126]. It is then possible to compare the band intensities of different transitions using only the Q-branches, henceforth denoted $Q(v', v'')$. Moreover, knowing the full Einstein coefficients $A'_v\ v''$ from one vibration state to another, the relative populations of different v states also can be found.

As seen in Figure 2.3, the measured spectral lines are in fact not lines but broadened Gaussian peaks centered at the wavelengths corresponding to the respective transitions. If the line shape in the spectrum is given by a function $L(\lambda)$, the corresponding

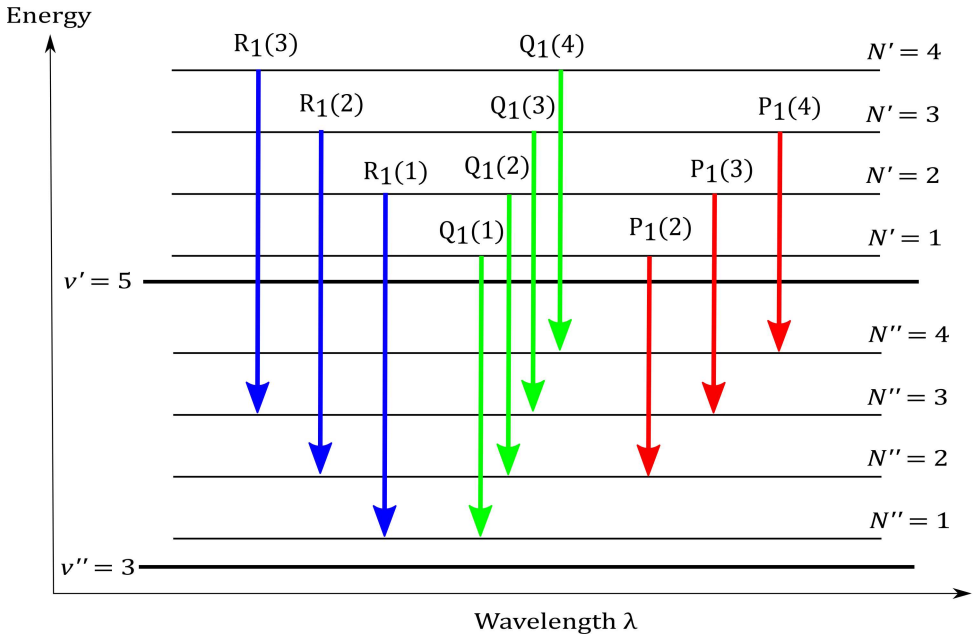

Figure 2.2: Energy diagram of the $(5, 3)$ transition band from the F_1 state showing the vibration and rotation levels with labeled transitions. The energy and wavelength axes are not to scale.

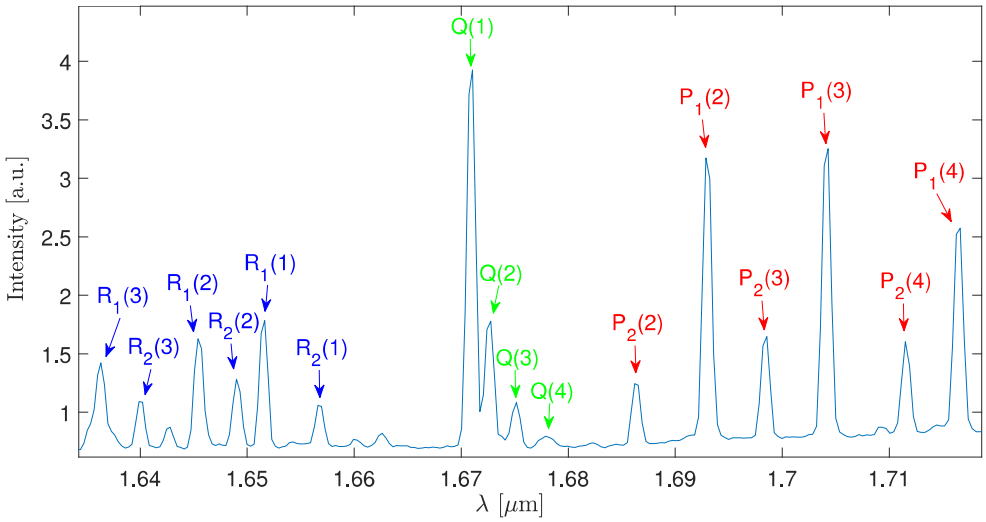

Figure 2.3: $(5, 3)$ transition band with labeled spectral lines. The intensity is given in arbitrary units. For the Q-branch, the spectral lines from sub-states F_1 and F_2 are on top of each other and the sub-script is therefore omitted.

line intensity I can be found by integrating $L(\lambda)$ over the wavelength interval $\Delta\lambda$ of the peak. That is,

$$I = \int_{\Delta\lambda} L(\lambda) d\lambda. \tag{2.19}$$

Figure 2.3 also illustrates that the Q-branch lines are close together, with a flatter part on

either side. This makes it possible to use the flat parts to fit a line to the noise structure, remove it and then use Equation (2.19) to evaluate the Q-branch intensity. For the P- and R-branch, the lines are further apart, which makes them less ideal for this study than the Q-branch. This methodology is discussed further in Section 4.1.5.

Chapter 3

Instrumentation

This chapter will provide an understanding of the properties and limitations of the instruments used to study the airglow trends. The Nordic Optical Telescope near-infrared Camera and spectrograph (NOTCam) is described in some detail in Section 3.1 and the Sounding of the Atmosphere using Broadband Emission Radiometry (SABER) experiment is briefly described in Section 3.2.

3.1 NOTCam

The main focus of this thesis is extracting and studying airglow trends using NOTCam. In this section, an overview of the Nordic Optical Telescope (NOT) and NOTCam is given before the data acquisition technique and some adverse effects are discussed. A description of the data format is also given.

3.1.1 Overview

The Nordic Optical Telescope is situated at Roque de los Muchachos Observatory, La Palma, Spain with coordinates N28°45′26.2″ E17°53′6.3″ and an altitude of $2382\,\mathrm{m}$ above sea level. The telescope is a Ritchey–Chretien optical system including several instruments to perform both imaging and spectroscopy [31, 32].

The Nordic Optical Telescope near-infrared Camera and spectrograph uses a slit and a combination of a prism and grating, called grism, to separate the incoming beam into its spectral components before being imaged on a 1024×1024 Rockwell Hawaii HgCdTe pixel detector. The detector is divided into 4 quadrants, each with an independent sub-detector differing slightly in characteristics. The instrument has a wavelength range from $0.8\,\mu\mathrm{m}$ to $2.5\,\mu\mathrm{m}$ and the ability to perform both high- and low-resolution spectroscopy with different slit lengths and widths. Several filters, also referred to as bands, are available in the low-resolution mode. In this thesis, the H, and K filters are used to extract the intensities of the $(3,1)$, $(4,2)$, $(5,3)$, $(6,4)$ and $(9,7)$ transitions. The wavelength ranges of the two bands are given in Table 3.1 and filter shapes are shown in Figure 3.2 together

Table 3.1: NOTCam low-resolution spectroscopy filters with wavelength ranges [33].

Filter	Wavelength range [μm]
H	1.48 to 1.78
K	1.95 to 2.37

with OH emission lines that are covered by each filter.

The low-resolution mode offers a spectral resolution $R = 2500$, which is high enough to resolve the OH spectral lines. A slit with length $4'$ and width $0.6'$ is used. The slit size corresponds to the angular resolution of the instrument, which means that at $90\,\mathrm{km}$ altitude approximately $100\,\mathrm{m}$ of the sky is covered in the field of view with a spatial resolution of $\frac{100\,\mathrm{m}}{1024} \approx 10\,\mathrm{cm}$ per pixel.

3.1.2 Data Acquisition

The 1024×1024 Rockwell Hawaii HgCdTe pixel detector consists of an array of HgCdTe photodiodes on top of an array of Si-based circuitry for photoelectron readout. In this configuration, each HgCdTe pixel with circuitry forms a closed loop with applied voltage V_a, pixel capacitance C, resistance R and a reset switch S. In its simplest form, the photoelectron readout is done by a voltmeter across the pixel capacitor as shown in Figure 3.1. When an observation commences the reset switch is opened. Incoming photons produce photoelectrons that will discharge the pixel capacitor leading to a voltage drop $dV = dQ/C$, where dQ is the amount of discharge caused by the photoelectrons. Note that the voltage V can be read without interfering with the detector. This is referred to as non-destructive readout. A certain amount of voltage drop dV will be registered as an analog-to-digital unit (ADU) which can be calibrated to photon count. In reality, the nature of the photodiode and photoelectron counter is more sophisticated than presented here, but the above serves to explain the principle of photon detection at the NOTCam.

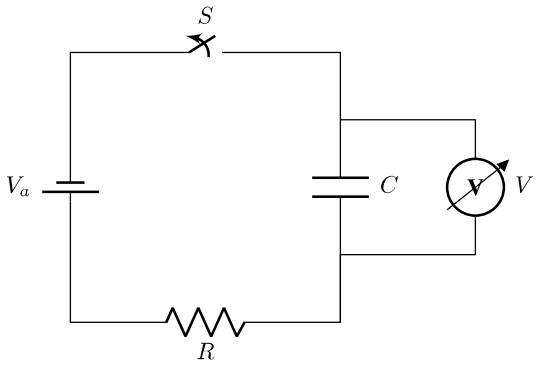

Figure 3.1: Concept drawing of a detector pixel circuit. A HgCdTe pixel is represented as a capacitor C with back-end circuitry including a reset switch S, an applied voltage V_a and some resistance R. The circuit is designed to read the voltage V across the pixel as the capacitor is discharged by photoelectrons hits.

NOTCam offers two readout modes. The first, called reset-read-read mode, opens the

reset switch S then immediately reads out the voltage V. The detector is then discharged by photoelectrons during the given exposure time before the voltage V is finally read once more at the end. The voltage difference between the two readouts will then be proportional to the number of photons hitting the detector during the time interval.

In the second mode, ramp-sampling mode, the voltage V is read multiple times during the exposure time to reduce the noise. At the beginning of the observation, the reset switch S is opened followed by a readout of the voltage V. Now, contrary to the reset-read-read mode, the voltage V is read out N times during the exposure. At the end of the observation, the total voltage drop dV is found by performing a linear regression between the N samples to obtain a mean discharge rate hence reducing the readout noise by a factor $\sqrt{N}$. Ramp-sampling is the mode used for the data analyzed in this project.

3.1.3 Non-linearity, saturation and memory effects

Ideally, the detector would have a linear response to incoming photons, meaning that a photon hit would always translate to the same number of ADUs. However, the detector does, in fact, have a non-linear response which increases with the amount of discharge dQ. For small discharges the off-set is negligible, and the non-linearity will stay below $1\,\%$ for ADUs below $27\,000$. Saturation occurs for ADUs exceeding 56000 [34]. If a bright image is recorded the illuminated pixels may still hold some persistent charge in subsequent images. This is referred to as memory effects and may alter the data by up to $0.5\,\%$ [35].

3.1.4 Data format

NOTCam uses the flexible image transport system (FITS) for data storage. Each FITS file contains a header and the 1024×1024 image with the number of registered ADUs per pixel in the detector. In ramp-sampling mode, the image from each individual sample is also included. The header includes relevant information about the observation, such as time and date, telescope angle, exposure time, employed slit and sub-detector gain in $\frac{\mathrm{e}^-}{\mathrm{ADU}}$. A comprehensive description of the FITS header used at NOT can be found in [36]. An advantage of the FITS header is that it makes it easy to develop an algorithm to scan through the archive, look for files that satisfy certain conditions and use those in the data analysis.

3.2 SABER

The Sounding of the Atmosphere using Broadband Emission Radiometry (SABER) instrument is an infrared radiometer capable of performing limb emission scans of the atmosphere. The instrument is mounted on the Thermosphere-Ionosphere-Mesosphere Energetics and Dynamics (TIMED) satellite, which is in circular orbit at an altitude of $625\,\mathrm{km}$ with an orbital inclination of $74.1°$. The nodal regression rate is 720 degrees per year [37, 38, 39].

SABER offers 10 different filters in the wavelength range from $1.27\,\mu\mathrm{m}$ to $16.9\,\mu\mathrm{m}$. Two of the filters cover spectral ranges around $1.6\,\mu\mathrm{m}$ and $2.0\,\mu\mathrm{m}$. These filters are de-

signed for OH emission studies, and are used in this thesis for comparison and validation of the seasonal cycle obtained using NOTCam. The filter shapes are given in Figure 3.2. It is seen that the $1.6\,\mu\mathrm{m}$ band coincides with the H band from NOTCam, though the SABER band does not cover the Q-branches of the $(3,1)$ and $(6,4)$ transitions. The $2.0\,\mu\mathrm{m}$ band overlaps with the NOTCam K band, but has more influence from the $(8,6)$ transition than the $(9,7)$ transition which is studied by NOTCam.

In the limb emission scan, SABER measures the volume emission rate (VER) of OH in the two bands, and gives the altitude of the emission. On the SABER webpage [40], data can be requested and filtered by geographical coordinates, month and year. Data is then delivered in monthly bundles, which in this thesis is averaged to obtain monthly intensity means. Monthly bundles for every month from 2008 to 2018 in a zonal window from N23°45′ to N33°45′ is used. The data is delivered in a Network Common Data Form (netCDF) [41] format, which is a compact way of storing array-oriented data. Each netCDF file holds a variety of data arrays, where indexed values in different data arrays correspond to simultaneous measurements. That is, for given indices, the VER in the data arrays of the two OH emission bands correspond the altitude in the altitude data array.

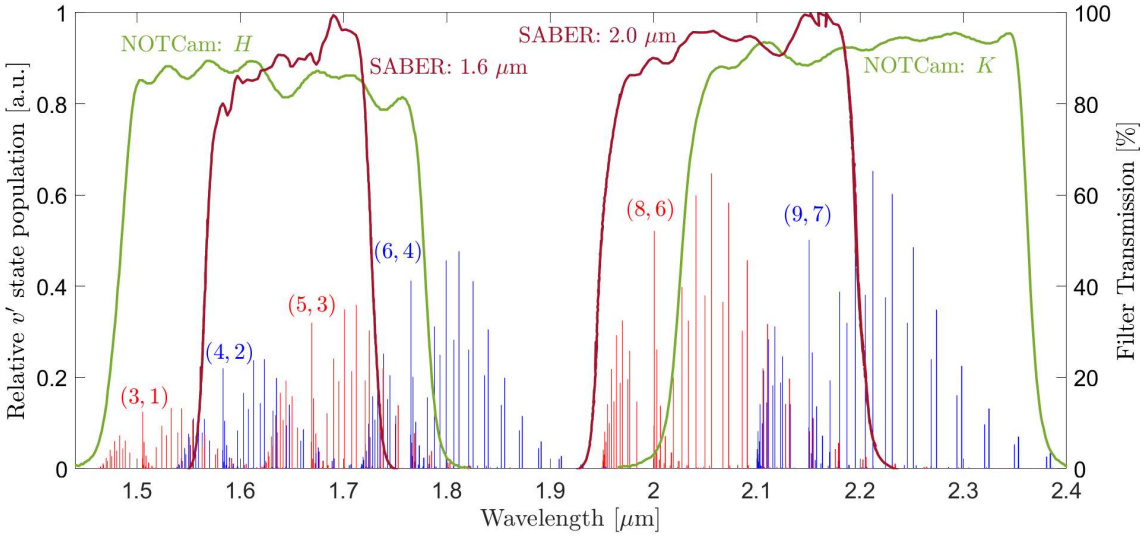

Figure 3.2: Filters used by NOTCam and SABER plotted together with positions of OH airglow emission lines. The emission lines are included to visualize the transitions that are covered by the two instruments. The line strengths are given in relative population of the upper v state and do not correspond to relative intensity.

Chapter 4

Implementation

This chapter describes the data processing and implementation that is done in order to extract the airglow intensities from the background of NOTCam data in Section 4.1 and how the SABER data was processed in order to obtain a seasonal cycle in Section 4.2.

4.1 NOTCam

NOTCam is primarily used to study astronomical objects in the near-infrared. This section describes how the astronomical object is removed from original image and how the airglow emission lines are extracted.

4.1.1 Raw image

A typical raw image is shown in Figure 4.1. The x-axis is spatial dimension, that is distance on the sky, and the y-axis is the spectral dimension where wavelength decreases with increasing pixel number. In the raw image, each pixel in the 1024×1024 image is given in ADUs. The first step of the signal processing is to divide each pixel value by the exposure time to get the intensity in ADU/s. The image is represented as a heat map where bright pixels corresponds to intensities.

The bright vertical line at spatial pixel ~ 425 is from an astronomical object confined to one point on the sky, and the slightly curved horizontal lines are from the OH layer extending over the whole spatial direction. The curvature is due to optical effects in the telescope which will be corrected in accordance with the method given in Section 4.1.3. The image in Figure 4.1 is from the H band, and the Q-branch transitions of the horizontal OH lines are marked on the image. The raw images from the K band are in essence very similar, except that OH lines appear at different locations.

Some unwanted features are also present the raw image. Cosmic radiation hitting a pixel will cause to appear very bright. Another effect causing bright points in the image are hot pixels, which is an irregularity where some pixels have exceptionally high offsets or thermal noise that causes them to become saturated. Bad pixels are also seen as dark

spots in the upper left corner and the "blob" at pixel coordinate $(150, 500)$. The positions of the bad pixels are well-known and pixel masks are available at the NOTCam webpage [42]. The dark vertical and the bright horizontal line forming a cross in the image is caused by irregularities at the boundary between the four sub-detectors.

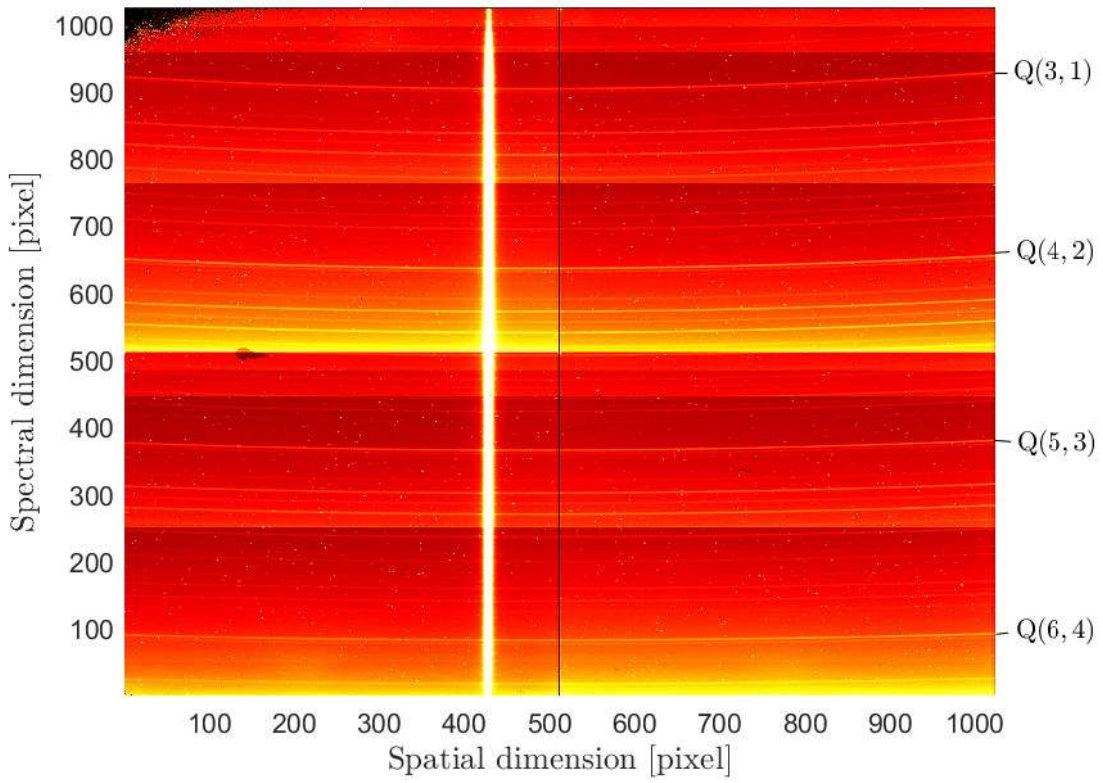

Figure 4.1: Raw image from the NOTCam represented as a heat map where bright pixels corresponds to high intensity. The x- and y-axes are spatial and spectral dimensions respectively. The bright vertical line is a celestial object and the bright horizontal lines are from the OH layer.

4.1.2 Dark frames

A dark frame is obtained by covering the telescope aperture and exposing the detector to complete darkness. This image will then represent the dark current in the detector and is subtracted from the raw image. Hot pixels are also easily identified from the dark frame and removed from the raw image. The dark frame corresponding to the raw image shown in Figure 4.1 is given in Figure 4.2(a). Most of the bright pixels are seen at the same locations in the raw image and dark frame. To further illustrate the spectral properties relating the two images, a spectrum of the raw image and dark frame is produced by adding up the spectral pixels in the horizontal direction. The spectra are given in Figure 4.2(b).

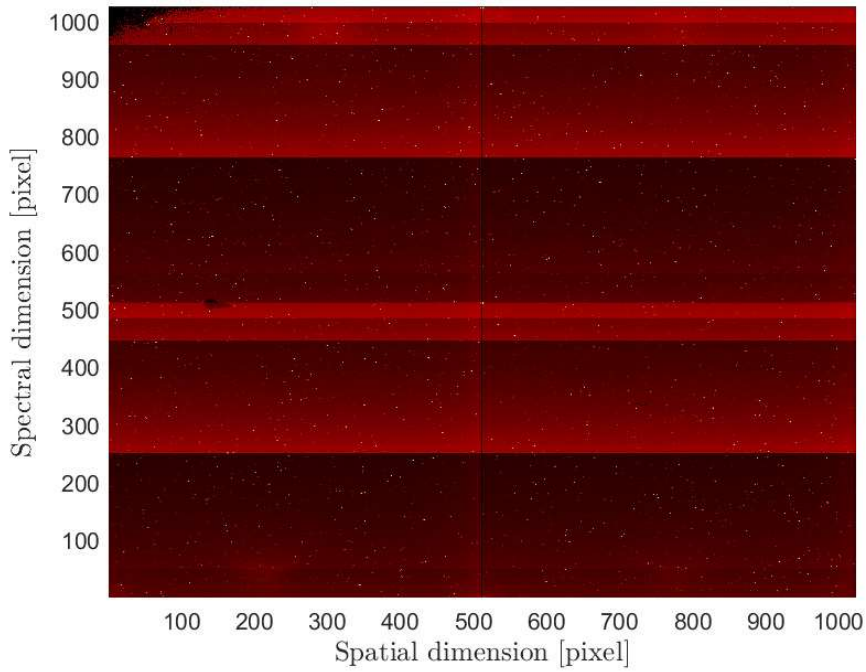

(a)

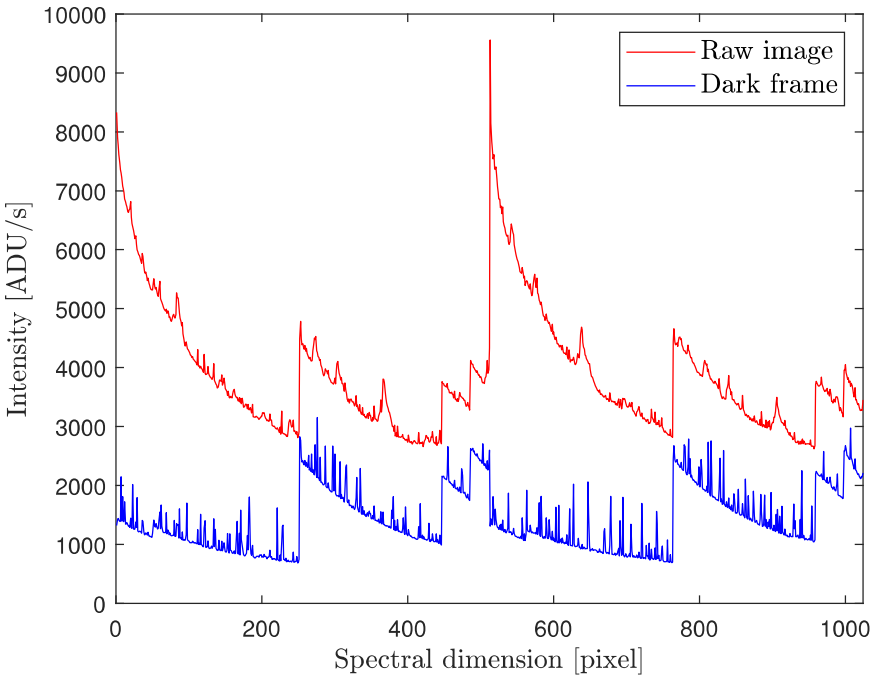

(b)

Figure 4.2: Dark frame corresponding to the raw image in Figure 4.1. A heat map representation is given in (a) while the raw image and dark frame is plotted together as a spectrum in(b) by adding up the spectral pixels in the spatial direction.

4.1.3 Image reduction

To get a good spectrum of the OH lines, the raw image is reduced in two steps. First, the bad and hot pixels are removed from the raw image together with cosmic hits. The pixels at the boundary between the 4 sub-detectors are also removed. Hot and bad pixels are removed using a pixel mask, and cosmic hits are identified by removing pixels that are brighter than certain thresholds. The dark frame is also subtracted and the vertical star is located and removed by applying a 60 pixel wide mask over it as shown in Figure 4.3. The star is located by scanning each vertical column, and recognizing the center of columns that are above a certain threshold brighter that the median column of the whole image as a star. Now, most of the single bright pixels are removed, but a few still remain. Ideally, they would all be removed, but since the unwanted pixels are chosen by a threshold value there is a trade-off between removing hot pixels and at the same time making sure the OH lines are not mistaken for cosmic hits. Consequently, a few bad pixels may be present in some of the images used and could introduce a small error if they appear to be on top of an OH line.

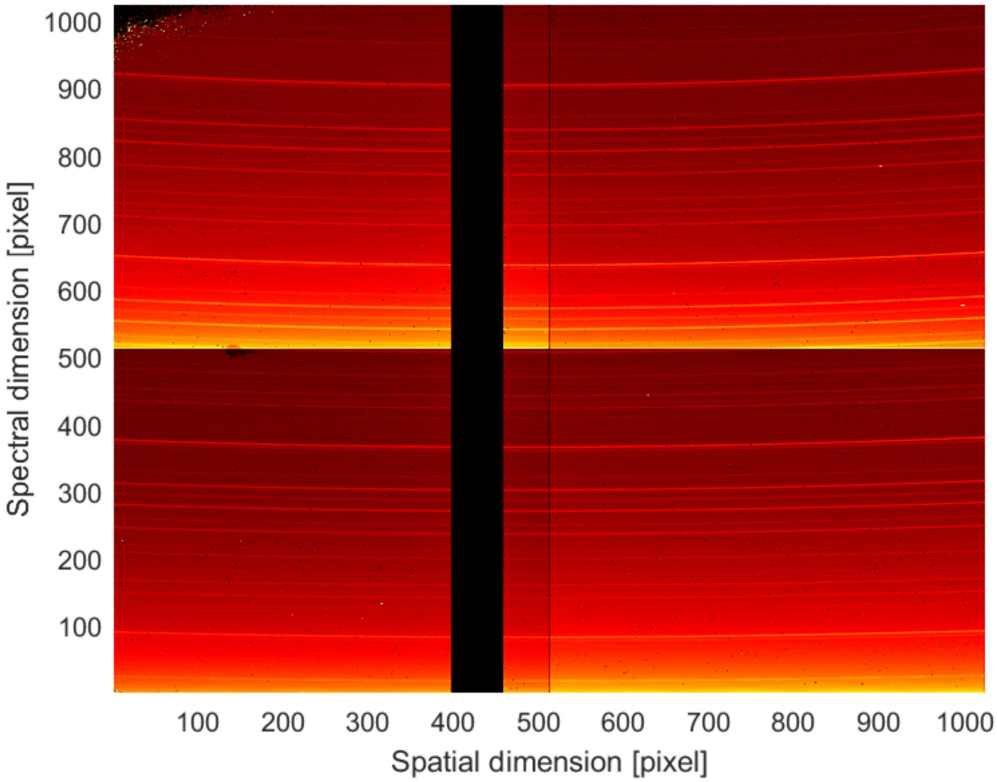

Figure 4.3: Raw image in Figure 4.1 after subtracting the dark frame in Figure 4.2(a), masking out the star and removing hot and bad pixels.

The second step in the image reduction is to linearize the curved OH lines. This is done in accordance with [43] making a transformation $(x, y) \rightarrow (x, y')$ from a frame where the OH lines are parabolic to a frame where they are linear. Here x and y are spatial and

spectral pixel respectively. The linearization equation is given by

$$y' = y + (x - p_1)^2 \cdot p_2, \tag{4.1}$$

where the coefficients p_1 and p_2 are found experimentally in [44] and given in Table 4.1. The linearized image is given in Figure 4.4. An unfortunate effect of the linearization process is the that last 24 pixels in both dimension are lost.

Table 4.1: Linearization coefficients.

Coefficient	Value
p_1	465
p_2	$3 \cdot 10^{-5} + 5.3 \cdot 10^{-8} \cdot y$

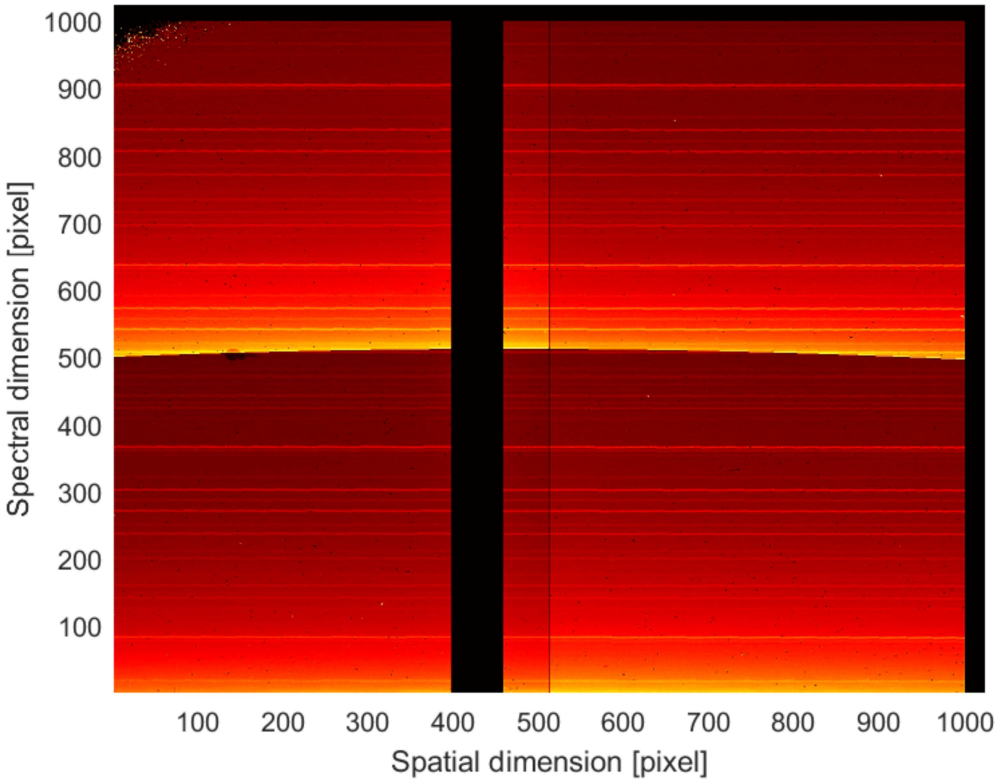

Figure 4.4: Linearized image.

Now that the image is cleaned and linearized, the spectrum can be obtained by adding up the intensities of each row in the spatial direction. The sum of removed pixels within a given row, S_r, varies from row to row. This is accounted for by assuming that the OH layer is constant within the field of view, and multiplying each row by a factor $\frac{1024}{1024-S_r}$. This yields a spectrum with intensity in units of $\mathrm{ADU/s}$ as shown in Figure 4.5.

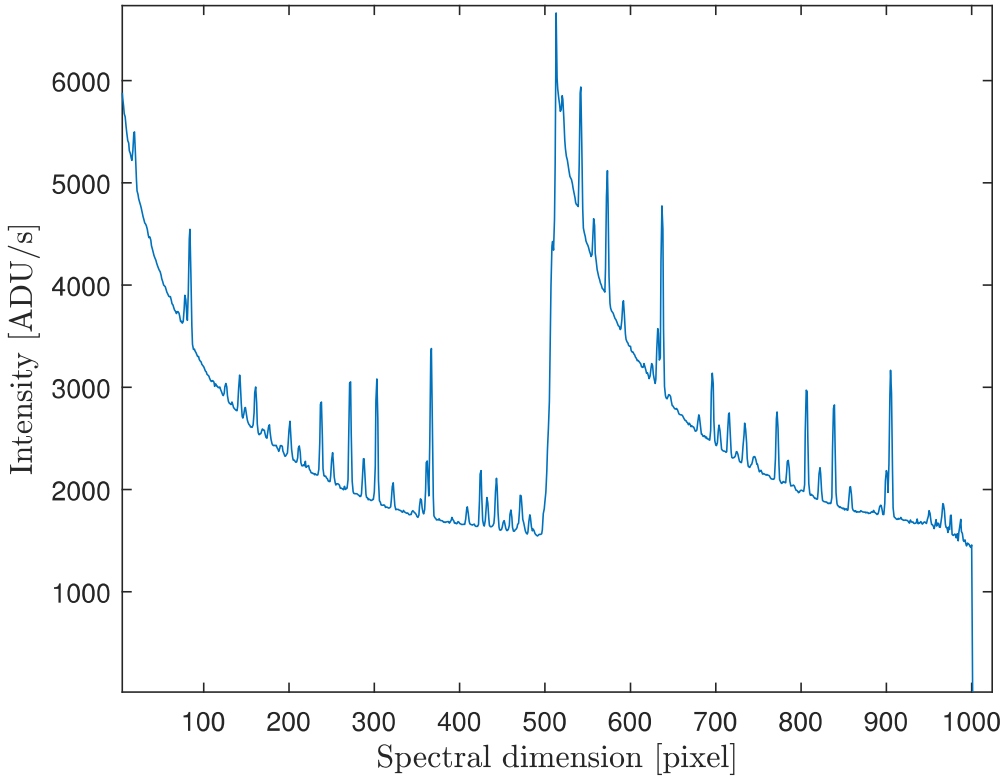

Figure 4.5: Uncalibrated 2D spectrum in the H band.

4.1.4 Calibration

The pixels along the spectral axis in Figure 4.5 can easily be calibrated to wavelengths, as the OH spectrum is meticulously studied and that wavelengths λ of each peak are well-known and catalogued [3]. Calibration is then done by adopting the method developed in [44, Section 5.2.2], where the spectral pixel number of a peak is identified and combined with the known wavelength of that peak to form several wavelength-pixel pairs which is used to perform a polynomial fit to compute a pixel to wavelength function. The resulting wavelength-pixel function is predominantly linear, with a small non-linear correction.

Converting the detector response $C(\text{pixel})$ in units ofADU/s/pixel to intensity emitted from OH layer in units $\text{photons}\,\text{s}^{-1}\,\text{sr}^{-1}\,\text{m}^{-2}\,\mu\text{m}^{-1}$ is done by obtaining the detector response of a calibration lamp of known spectral radiance $L(\lambda)$ that covers the field of view of the telescope. Such measurements are called flat fields and are normally used to correct for the relative differences in spectral response across the detector. In the following, a method using the flat field for absolute intensity calibration is presented.

The whole system with telescope, aperture, slit, grism, filter, and detector can be considered as a filter with input $L(\lambda)$, output $C(\text{pixel})$, and response function R as shown in Figure 4.6. Here, $L(\lambda)$ is the spectral radiance, in units $\text{photons}\,\text{s}^{-1}\,\text{sr}^{-1}\,\text{m}^{-2}\,\mu\text{m}^{-1}$, of a known source subtending the full solid angle of the field of view, and $C(\text{pixel})$ is detector output spectrum in units ADU/s as a function of spectral pixel for the known source.

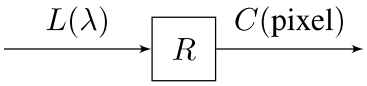

Figure 4.6: NOTCam as a simple filter structure where $L(\lambda)$ is the spectral radiance of a source subtending the full field of view, $C(\text{pixel})$ is the output given in the final image and R is a response function relating the input and output.

The response function R will then relate the two through

$$R = \frac{C(\text{pixel})}{L(\lambda)}, \tag{4.2}$$

and is found by illuminating the telescope using a Halogen lamp of known colour temperature $T = 3200\,\text{K}$. The input radiance $L(\lambda)$ is then given by

$$L(\lambda) = \frac{2 \cdot 10^{18}}{\lambda^4} \frac{1}{e^{10^6 \frac{hc}{\lambda k T}} - 1} \left[\text{photons}\,\text{s}^{-1}\,\text{sr}^{-1}\,\text{m}^{-2}\,\mu\text{m}^{-1}\right] \tag{4.3}$$

where h, c and k are given in Table 4.2 and T is the colour temperature of the Halogen lamp.

Table 4.2: Constants and units used in Equation 4.3.

Symbol	Name	Value
h	Plack's constant	$6.626\,069\,3 \times 10^{-34}\,\text{W}\,\text{s}^{-2}$
c	Speed of light	$2.997\,924\,58 \times 10^{8}\,\text{m}\,\text{s}^{-1}$
k	Boltzmann's constant	$1.380\,658 \times 10^{-23}\,\text{J}\,\text{K}^{-1}$

The detector output spectrum $C(\text{pixel})$ of the known source is obtained by following the data processing steps given in this chapter and the response function R is found using Equation 4.2. With the assumption that the detector system does not change, any measured spectrum $C(\text{pixel})$ of a an unknown source subtending the full field of view can be converted to spectral radiance $L(\lambda)$ using

$$L(\lambda) = \frac{C(\text{pixel})}{R}, \tag{4.4}$$

since both $C(\text{pixel})$ and R are known. As discussed in Section 5.1.2, this method for an absolute calibration is limited by the accuracy to which the absolute intensity of the calibration source is known. However, it is still a reliable way of obtaining the relative spectral response of the detector.

As a final step in the intensity calibration, the Van Rhijn effect [45, Page 534] is accounted for by dividing the intensity by the airmass. This is done to account for the fact that if the telescope is at an elevation angle θ relative to the horizon, the observed path length through the airglow layer increases, which will make the glow appear brighter. By dividing by the airmass, approximated to

$$\text{airmass} \approx \frac{1}{\sin\theta}, \tag{4.5}$$

the intensity is normalized to zenith and intensities measured at different telescope elevations can be compared. This approximation assumes a flat earth and an airglow layer of constant thickness. It is also assumed that the observed OH emission lines are not mitigated through atmospheric extinction and absorption.

4.1.5 Final spectrum

Now that the spectrum is calibrated, as shown in Figure 4.7, the intensities of the Q-branch is determined by locating the peaks associated with a transition, and assuming the shape of the noise floor on each side of the branch is continuous through the peaks. Then a line is fitted between the noise floors on both sides and subtracted from the branch. Finally, the intensity of the Q-branch peaks is integrated numerically using a Riemann sum. This is done for the Q$(3,1)$, Q$(4,2)$, Q$(5,3)$ and Q$(6,4)$ transitions in the H band, and Q$(9,7)$ transition in the K band.

For the noise floor shape, it was found that 2nd and 3rd degree polynomial fits both gave accurate fits for the samples with high signal to noise ratio, but made less accurate fits for the low signal to noise ratio samples. However, after inspecting several samples, it appears that when the 2nd degree fit results in an overestimation, the 3rd degree fit gives and underestimation, and vice versa. Therefore, the integration process was done with both the 2nd and 3rd fit and the resulting intensity is determined using the mean of the two. This also provides a basis for error estimation using the standard error of the two intensities. Figure 4.8 shows how the noise floor shape is found using the curve fits together with how the integration area is chosen.

Another error estimation was made based on the standard deviation σ of the noise on each side of the Q-branches after subtracting the noise floor shape. If σ is assumed to be constant within the integration area, the expected error of each intensity value and further the expected error of the integrated intensity can be approximated. The Riemann sum is given by

$$I = \sum_{i=1}^{N} I_i \cdot d\lambda, \tag{4.6}$$

where I is the integrated intensity, N is the number of pixels resolving the peak, $d\lambda$ is the wavelength range of a pixel and I_i is the value of the spectrum at pixel i. The error δI is then estimated using the principle of Gaussian error propagation, in this case given by

$$\delta I = \sqrt{\sum_{i=1}^{N} (\frac{\partial I}{\partial I_i} \delta I_i)^2}, \tag{4.7}$$

where δI_i is the uncertainty of each I_i which is assumed to be equal to σ. Equation (4.7) is then reduced to

$$\delta I = \sigma d\lambda \sqrt{N}. \tag{4.8}$$

Finally, the largest of the error estimate made using the difference of the two noise floor fits and the error estimate made using Gaussian error propagation was used as the final error estimate for the given sample.

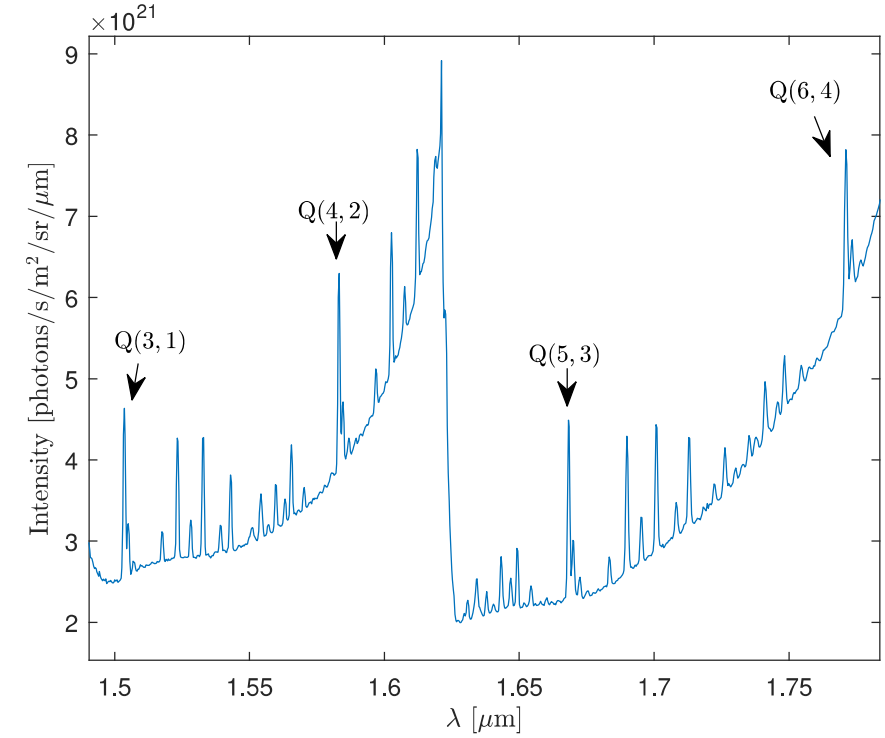

(a) H band spectrum

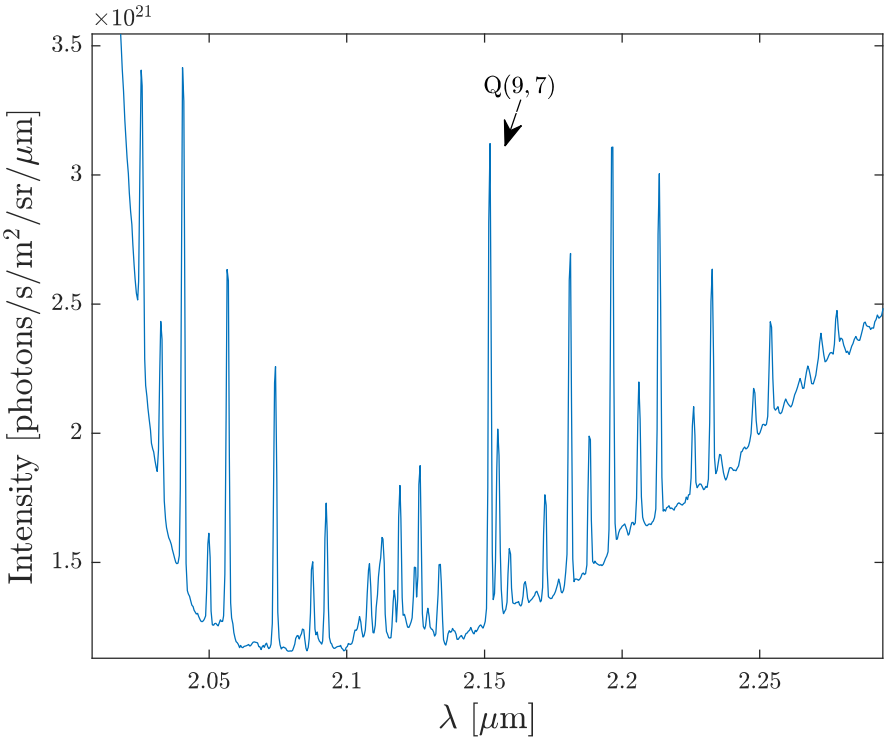

(b) K band spectrum

Figure 4.7: Calibrated H band spectrum (a) and K band spectrum (b).

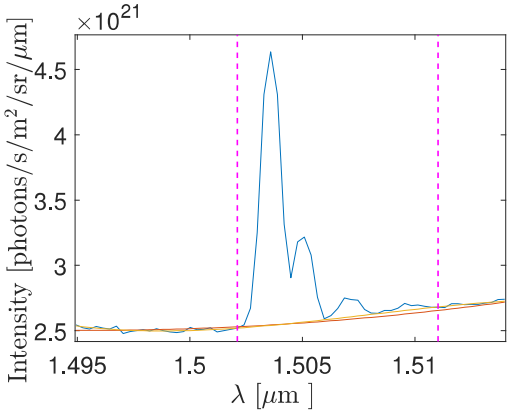

(a) Q(3, 1).

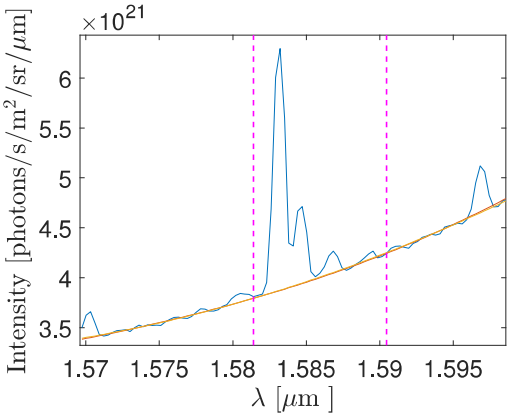

(b) Q(4, 2).

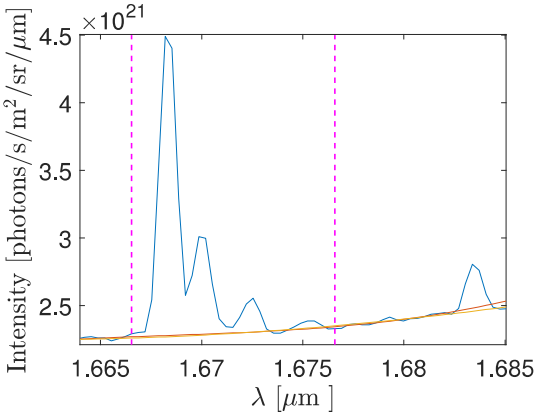

(c) Q(5, 3).

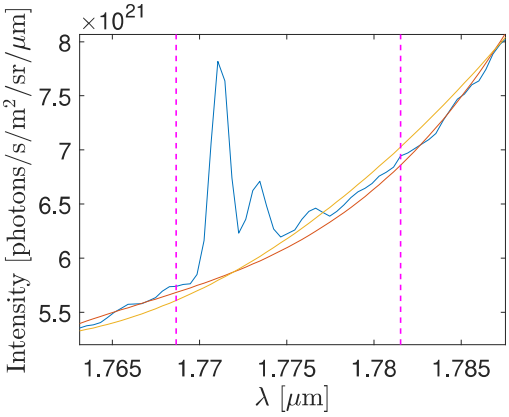

(d) Q(6, 4).

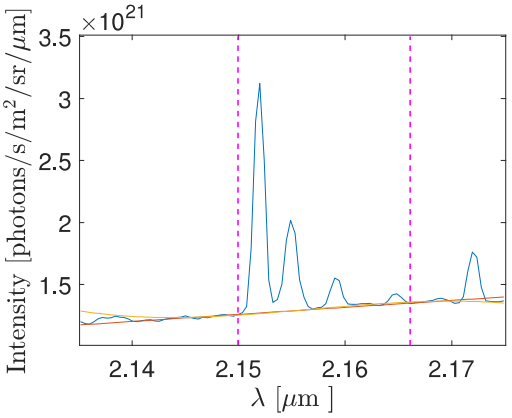

(e) Q(9, 7).

Figure 4.8: Noise floor fit of the Q-branch for the transitions in the H and K band. The vertical dashed lines mark the Q-branch and integration area. The red line is the 2nd degree noise floor fit, and the yellow line is the 3rd degree fit.

4.1.6 Note on dark frames and flat fields

The data processing techniques discussed so far in this chapter rely on having dark frames and flat fields taken the same night as the observation. For the dark frames, not only should they be from the same night, but they should also be imaged with the same ramp-sampling mode as the raw image. That is, they should have the same number of readouts and exopsure time per readout, as described in Section 3.1.2. Dark frames and flat fields that satisfy these conditions are hereafter referred to as proper or specific dark frames and flat fields, but they are not always available when the whole data set from 2008 to 2016 is considered. An analysis was therefore performed to see whether a mean of all available dark frames and flat fields, referred to as a master dark frame and master flat field, could be used as a substitute when proper dark frames and flat fields were missing.

4.1.7 Automation

So far, the data reduction steps for a single observation is given. It requires having a dark frame, a flat field, and locating the Q-branch peaks for integration. This is easily done by hand for a single observations, but when there are hundreds of samples, selecting dark frames, flat fields and integration areas by hands becomes infeasible. Therefore, an algorithm was constructed that automatically scans through the archive and autonomously selects dark frames, finds the Q-branches and integration areas and outputs the intensities and time of observation for each sample. The rest of this section is a short introduction to the developed algorithm and will be relevant primarily for readers desiring an introduction to the coding framework before adapting and advancing it. A repository with all files used is available in [46].

First, two lists of the file names of FITS files containing raw images in the H and K band were created by implementing a function that scans through the archive and reads the FITS header of every file. From the FITS header of each file, the filter can be determined, and files that are imaged using spectroscopy, and are not dark frames or flat fields, are identified as raw images of astronomical objects and added to its respective list. Dark frames and flat fields will have keywords such as “dframes”, “Ha”, “Halogen” and “flat” and are easily identified.

Secondly, the intensities where extracted by implementing a function that scans through those lists of raw images. The night of observation and ramp-sampling mode is extracted from the FITS header, and used to check of if there are any dark frames available from that night with the corresponding ramp-sampling mode. If there are, the mean of the available dark frames is used to subtract the dark current from the raw image. If there are no proper dark frames available, a master dark frame is used as a substitute. Very few flat fields were available for both the H filter and K filter. Therefore, a master flat field was created by taking the mean of all available flat fields for the H filter and K filter respectively. The raw image is then processed in accordance with the image reduction steps describer earlier in this chapter.

The third step is locating the Q-branches and performing the numerical integration. This is done by realizing that the peaks appear at roughly the same pixel numbers for all samples, and using a peak location function in that range. The dispersion of the detector is also constant. That means that a given wavelength range will have a constant pixel range.

Thus, if it is known that the wavelength of the $\mathrm{Q}(1)$, that is the most prominent Q-branch emission line, of the $(3, 1)$ transition is at a certain pixel number, the integration range of the $\mathrm{Q}(3, 1)$ can be set relative to that pixel. The $\mathrm{Q}(1)$ of the other transitions in the H band, and their integration ranges, can also be set relative the the pixel number of the $\mathrm{Q}(1)$ of the $\mathrm{Q}(3, 1)$ transition. Thereafter, the noise floor fit lines showed in Figure 4.8 were implemented. The flat areas on either sides of the Q-branches were used, and the specific noise floor fit ranges where also set relative to the identified pixel number of the most prominent peak. Pixel numbers were emission lines from other atmospheric species occur are identified by inspecting samples with long exposure time, and can then be skipped by the line fit functions. The procedure in the K band is in essence identical.

Finally, the integrated Q-branch intensities can be outputted together with a time stamp in coordinated universal time (UTC). The time stamp is collected from the FITS header, and is straight-forward to convert to local solar time, hours past sunset or other time dependent parameters based on the geographical coordinates of the NOT and the time of year.

4.2 SABER

The monthly netCDF file contains data arrays holding the OH emission rates and corresponding altitudes. As the filter shapes from Figure 3.2 are already accounted for when the data is delivered, no processing is needed for the raw data. The arrays are formatted such that each column corresponds to a vertical scan of the atmosphere. When the data was acquired from the SABER webpage, it was pre-filtered to only contain nighttime observations in the latitude range from N23°45′ to N33°45′, but including all longitudes. In other words, a zonal nighttime mean. Data from every month of the year in the 11 years from 2008 to 2018 was used, and the months were combined to obtain a seasonal cycle of the airglow intensity. It was assumed that by combining data from the 11 years, each month would have an unbiased distribution of observations. More precisely, it is assumed that the observations are evenly distributed over the selected latitudes and longitudes, and that all local solar times are well represented. This was not checked explicitly, but it can be done by converting the orbit parameters that are available in the netCDF file to geographical coordinates and local solar time.

As each column in the data arrays correspond to a vertical scan of the atmosphere, the mean monthly vertical profile of the airglow VER in the $1.6\,\mu\mathrm{m}$ and $2.0\,\mu\mathrm{m}$ bands can be obtained by taking the mean of each row in the data arrays. This results in three columns. Two VER columns and one column with corresponding altitudes which represent the the mean values of that month. This is possible because each row correspond to approximately the same altitude above a fixed geographical coordinate. An example of such a mean monthly vertical profile is given in Figure 4.9. In order to transform the profile into a quantity than can be compared with the NOTCam measurements, the OH volume emissions rates were integrated along the altitude. The result will then be in units of ergs $\mathrm{cm}^{-2}\,\mathrm{s}^{-1}$, which can be interpreted as surface brightness and is proportional to the NOTCam intensities.

The final product is then monthly intensity means from 11 years. The mean of the respective months from all available years are used to obtain the seasonal cycle, and the

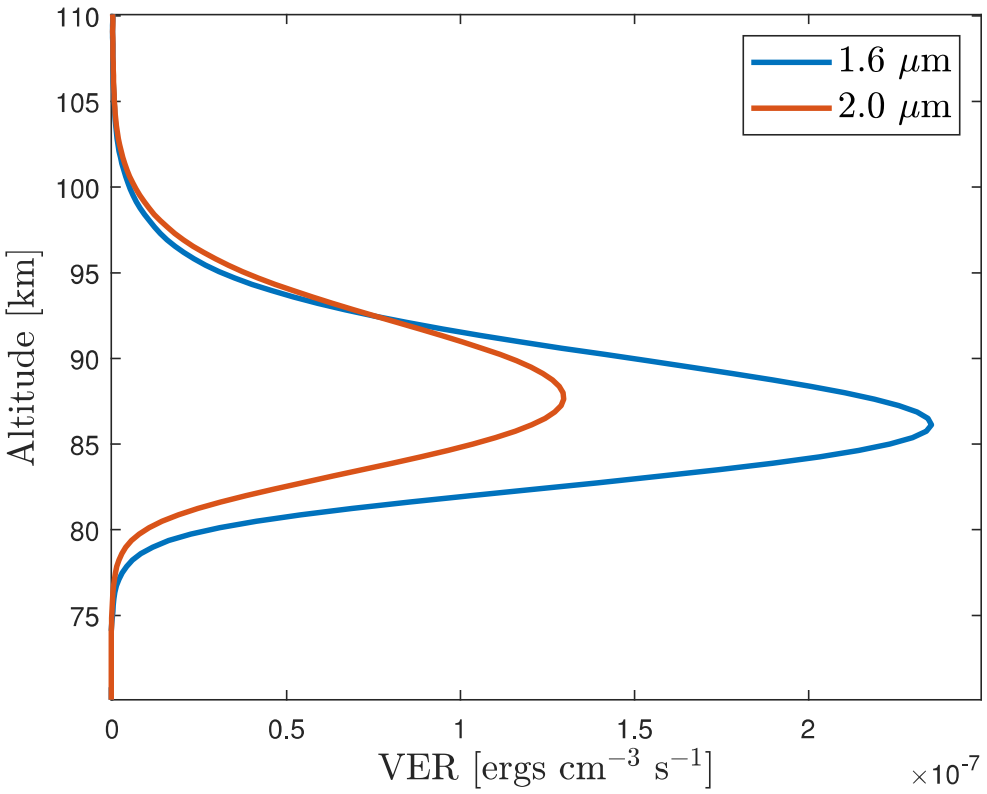

Figure 4.9: SABER OH vertical emission rate (VER) as a function of altitude for the $1.6\,\mu\mathrm{m}$ and $2.0\,\mu\mathrm{m}$ band. The pictured profile is the mean monthly profile from May 2013, from a 10° zonal mean centered at N28°45′.

standard error of the mean is used as an error estimate for each month. As the intensity units of SABER and NOTCam are not identical, albeit proportional, the seasonal cycles are analyzed by looking at the percentage deviation from annual mean (PDFAM), given by

$$\text{PDFAM} = \left(\frac{\text{monthly intensity}}{\text{annual mean intensity}} - 1 \right) \cdot 100\%. \tag{4.9}$$

Chapter 5

Results and discussion

In this chapter, the results are presented and discussed. First, an initial discussion and analysis of the assumptions made regarding the dark frames and flat fields is given, before an inspection of the acquired Q-branch intensities in the H and K band. Thereafter, the resulting airglow trends are presented, before a discussion on the impact of including observations with high airmasses is given.

5.1 Initial data validation

This section provides a preliminary analysis of the dark frames, flat fields and extracted Q-branch intensities.

5.1.1 Dark frame analysis

A plot of all the dark frame spectra is given in Figure 5.1(a). As the detector is cooled with liquid nitrogen and is assumed to remain constant, the dark frames were expected to yield stable spectra without considerable deviations from spectrum to spectrum. However, Figure 5.1(a) shows that this is not the case. The spectra do vary in overall intensity, though the general shape seems to be constant even though there are a few exceptions. The relative intensity development of the dark frames is plotted in Figure 5.1(b). There is no apparent correlation between intensity and time, and the dark frames show erratic and unpredictable characteristics.

In conclusion, the dark frames vary a lot between nights and only dark frames taken the same night as the observation should be used to subtract the dark current. However, as the general shape of the dark frames remains constant, an analysis was carried out to check if a mean of all the dark frames, also referred to as a master dark frame, can be used to approximate the dark current and identify hot pixels for observations where dark frames taken the same night with the same ramp-sampling mode, referred to as proper dark frames, are missing. In order to estimate the relative error introduced when using a master dark frame instead of a proper dark frame, intensity readings of samples where

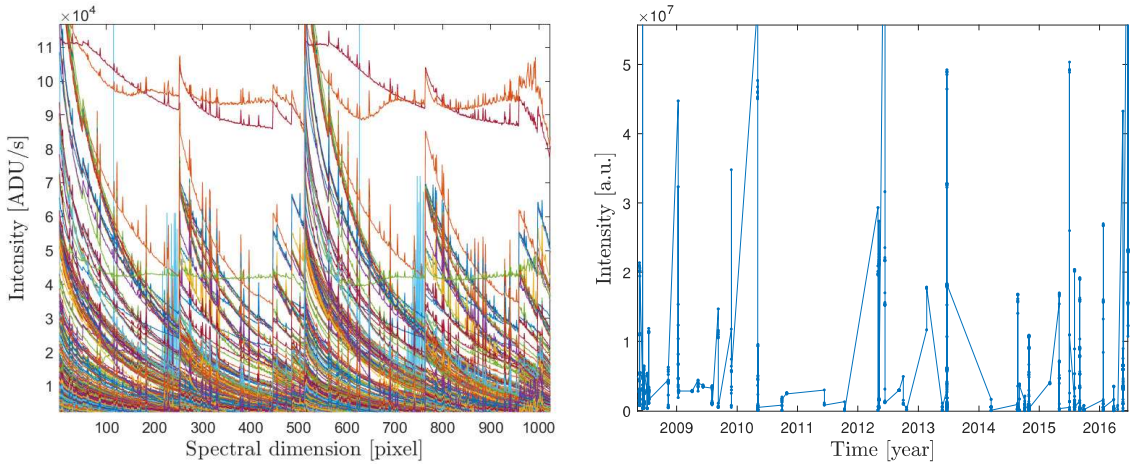

(a) Dark frame spectra.

(b) Dark frame intensity.

Figure 5.1: Spectra (a) and intensity development (b) for all available dark frames.

proper dark frames exist where compared with the corresponding intensity readings of the same samples when a master dark frame was used instead.

The relative difference between the two intensities, given by

$$\text{Relative difference} = \frac{\text{Intensity using master dark frame}}{\text{Intensity using proper dark frame}} - 1, \tag{5.1}$$

will then be an estimate of the relative error that must be accounted for when using a master dark frame. Figure 5.2 shows the distributions of relative difference plotted together with a normal distribution fit. For the H band, the Q-branch intensities of the $(3,1)$, $(4,2)$, $(5,3)$ and $(6,4)$ transitions are used, and for the K band the Q-branch intensity of the $(9,7)$ transition is used.

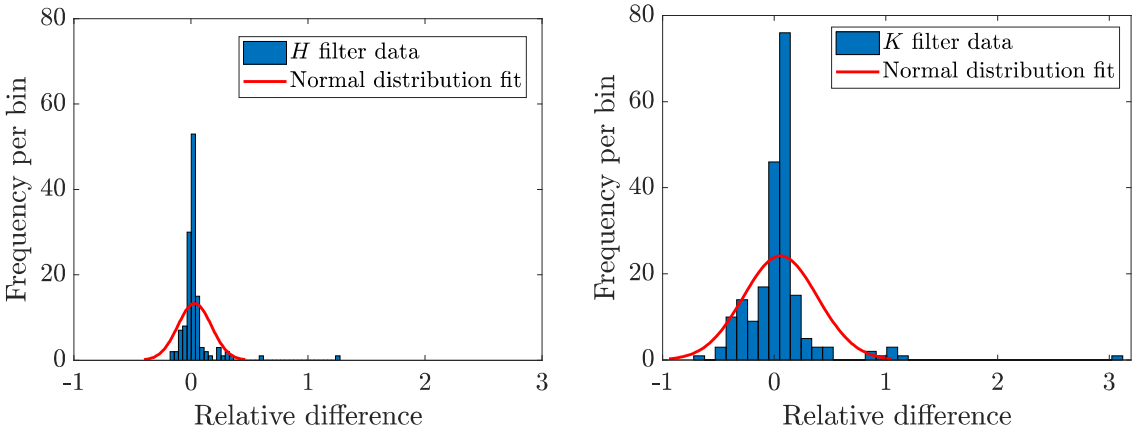

(a) H band.

(b) K band.

Figure 5.2: Relative differences between intensities obtained with proper dark frames and a master dark frame for the H and K band. The bin widths are different in the two plots, so the bar heights cannot be compared. However, the normal distribution fits are comparable.

The relative intensity differences between samples using the proper dark frame and the master dark frame appear to form a narrower and taller normal distribution centered around 0. There are a few outliers at relative differences above $50\,\%$. For a statistical analysis, Table 5.1 states the standard deviation, mean absolute deviation and root-mean squared deviation of the two distributions. The mean absolute deviation is obtained by taking the absolute value of the relative differences and finding the respective averages of those differences for the two distributions.

Table 5.1: Standard deviation STD, mean absolute deviation MAD and root-mean-square deviation RMSD of the relative difference distributions.

	STD	MAD	RMSD
H band	0.14	0.06	0.15
K band	0.33	0.18	0.34

As the distribution of relative differences is taller and narrower than the fitted normal distribution, the standard deviation and the RMSD are probably over-estimates of the relative error accumulated when using a master dark frame. Thus, the mean absolute error is used as an error estimate. Consequently, a relative error of $6\,\%$ and $18\,\%$ is added to the H and K filter intensities, respectively, when the master dark frame had to be used.

5.1.2 Flat field analysis

The flat fields used to obtain the response function of the telescope are critical for intensity calibration. With the assumption that the detector and telescope remains constant the flat field spectra should also be constant. A plot of all available flat fields in the H and K band is given in Figure 5.3(a) and Figure 5.3(c). It is clearly seen that the spectrum does vary in overall intensity, though the shape remains constant. To check the time dependency of the intensity variation, the intensities per spectral pixel were added together to get a number representing the total intensity of the respective flat fields, which are plotted versus time in Figure 5.3(b) and Figure 5.3(d). The total intensity variation seems to be random in time, though the H and K intensities appears to be somewhat connected.

It is thus concluded that the flat fields should not be used for absolute calibration, as it is unlikely that the detector response varies randomly. However, as the shape is preserved, the flat fields serve well as a relative calibration for the detector response. All intensities reported in this thesis should therefore be read as relative intensities in arbitrary units (a.u.). The fact that intensities obtained by using the flat fields as a means of absolute intensity calibration gave intensities several orders of magnitude larger than than found in for example [3], [47] and [48] is also a strong indication that the flat fields should only be used for relative intensity calibration.

A mean of the flat fields in Figure 5.3(a) and Figure 5.3(c) were used to create two master flat fields for the H and K band. It is further assumed that the total intensity of the H and K master flat fields represent the detector under the same conditions, such that the intensities of the H band and K band can be compared, even though they are given in arbitrary units. This assumption is largely based on the qualitative similarities of Figure 5.3(b) and Figure 5.3(d). An estimate of the quantitative accuracy of this assumption

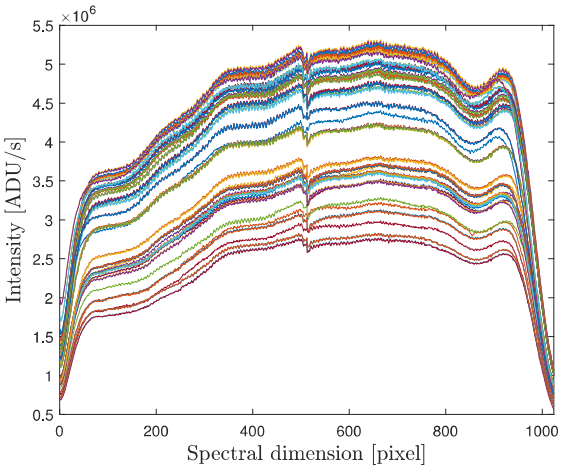

(a) Flat field spectra in the H band.

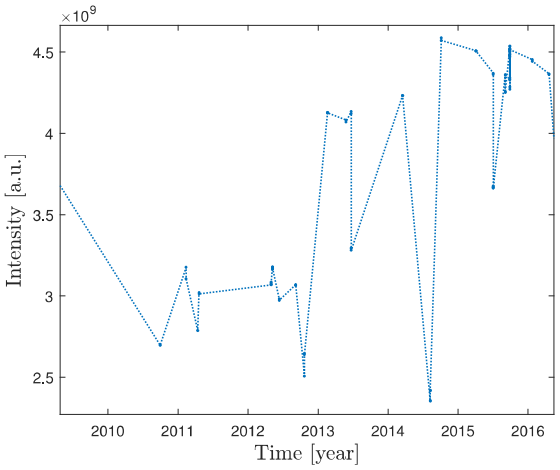

(b) Flat field intensity in the H band.

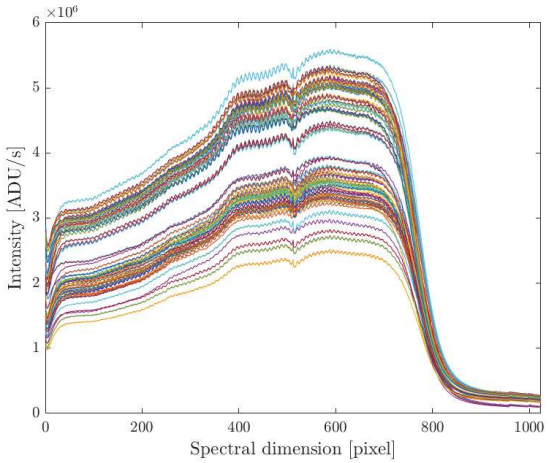

(c) Flat field spectra in the K band.

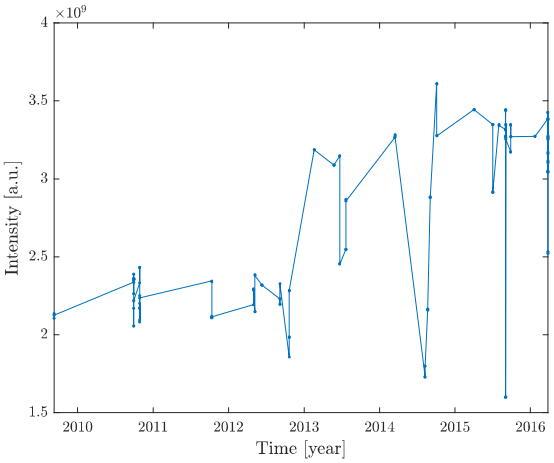

(d) Flat field intensity in K band.

Figure 5.3: Flat field spectra and intensity development over time for in the H and K band.

has not been made, and comparisons between the $(3, 1)$, $(4, 2)$, $(5, 3)$ and $(6, 4)$ transitions in the H band relative to the $(9, 7)$ transition in the K band should be made with caution. However, the intensities of the transitions within the H band can be evaluated relative to each other with greater certainty as they are calibrated using the same master flat field.

Reasons for why the flat fields vary and yield absolute intensities that are too high could be that for the calibration to work it is assumed that a source of known black-body temperature is subtends the whole field of view and aperture of the telescope, though in practice, a Halogen lamp in the observatory shines light which is diffusely reflected from the ceiling down onto the telescope system. It is likely that the reflectivity of the ceiling is less than 1. Additionally, if the reflection is not fully diffuse, the full field of view will not be filled. Consequently, the light received can be much lower than assumed in Equation (4.3), which will result in a response function that is too low and ultimately cause an overestimation of the unknown source using Equation (4.4). Any change in the

in the environment inside the observatory will also lead to changes in how the light is reflected and absorbed on surfaces and equipment. The fact that the intensity fluctuations in Figure 5.3(b) and Figure 5.3(d) appear random in time, but connected with each other is further evidence that the surroundings affects the measurements here. If measurements in the H and K band are taken in similar time periods this is a behavior that could be expected.

5.1.3 Initial inspection of Q-branch intensities

H band

A total of 442 observations in the time frame from 2008 to 2016 were used to analyze the Q-branch intensities of the $(3,1)$, $(4,2)$, $(5,3)$ and $(6,4)$ transitions which are present in the H filter band of the NOTCam. The whole data set is presented in Figure 5.4. The most important features to note from Figure 5.4 is that there are large gaps between observations and that the intensity variations during single observation nights are of the same magnitude as any indication of long-term variations.

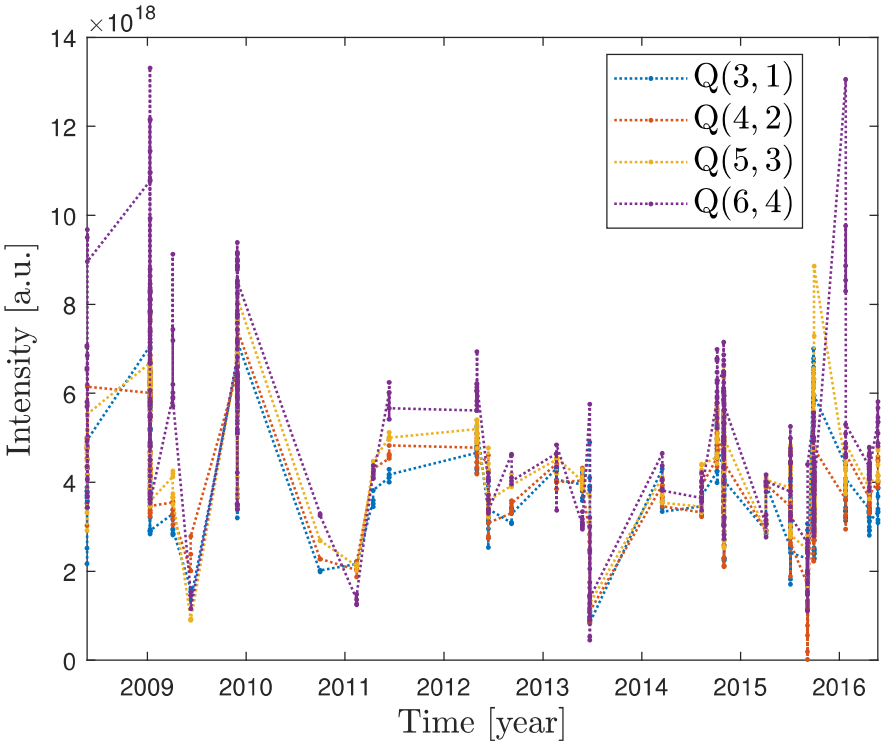

Figure 5.4: Q-branch intensities of the $(3,1)$, $(4,2)$, $(5,3)$ and $(6,4)$ transitions plotted over time without error bars.

Figure 5.5(a) and Figure 5.5(b) show the intensity variation for two nights. Notice the relatively steep intensity increase towards sunrise in the latter. There are two main conclusions to be drawn from these plots. Firstly, due to the high variability for each night, it is evident that having a good distribution of data for all hours of the night is needed to accu-

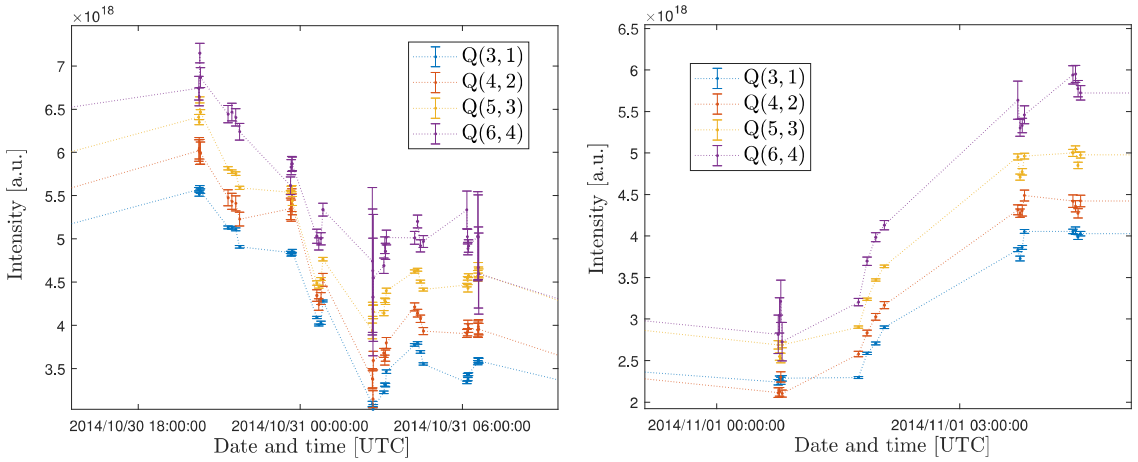

Figure 5.5: Intensity development for two nights plotted with error bars. Notice the large magnitude of the variation in (a) and (b) and the sharp increase in intensity towards dawn in (b).

rately study long-term trends in intensity. Secondly, there is clear coherence between the intensity variations of the different transition bands (v', v''). They rise and fall with each other, and seem to maintain a constant ratio. This indicates that meaningful information regarding the OH layer can be extracted from the background of the NOTCam spectra.

The coherent behavior of the relative intensities of the four bands is further highlighted when the intensities are plotted as a function of observation number, or index, instead of time as in Figure 5.6. The index will be strictly increasing with time towards the right, but not linearly. Nevertheless, the general structure of the OH band variance is shown, and it is again seen that the different Q-branch intensities follow each other in an orderly fashion. In order to visualize the uncertainty of the intensities, a highlighted range of Figure 5.6(a) is given with error bars in Figure 5.6(b). The correlation between the relative intensities are once more confirmed, though there are some irregularities. In Figure 5.6(b) it is seen that the intensities are often regular with relatively small error bars, but some samples have higher uncertainty, as seen especially for the $\mathrm{Q}(6, 4)$ intensities after observation index 300. Reasons for the high uncertainties could be short exposure times, lack of proper dark frames or an irregular background noise structure that is difficult to subtract accurately.

The different Q-branch intensities in the H band were divided by the $\mathrm{Q}(3, 1)$ band intensities and plotted in Figure 5.7 to analyse the relative intensities. There appears to be a trend towards the $\mathrm{Q}(6, 4)$ band being the most intense, followed by $\mathrm{Q}(5, 3)$, $\mathrm{Q}(4, 2)$ and finally $\mathrm{Q}(3, 1)$. However, large deviations are also observed and it is not clear whether the ratio $I_{(v',v'')}/I_{(3,1)}$ is constant or fluctuating. It is also seen in Figure 5.7(b) that large deviations from the ratio trends are associated with large error bars. Another argument to be made is that the regions where the intensity ratios are constant correspond to times when the species involved in Equation (2.14) are in some steady-state or equilibrium relative to each other. Ratio fluctuation, on the other hand, could then be a result of the fluctuations in for example atomic oxygen O which has a v dependent quenching rate.

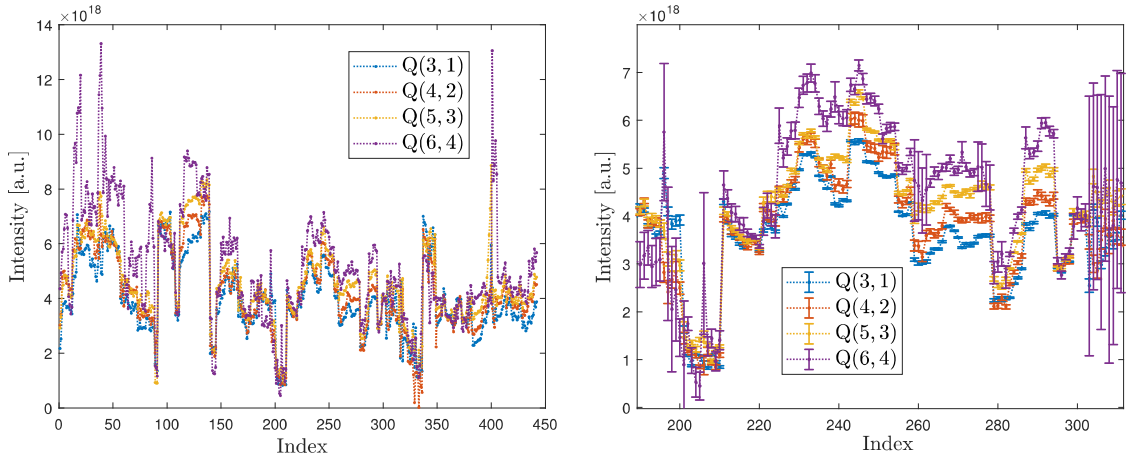

(a) (b)

Figure 5.6: Q-branch intensities as a function of observation index. The full set of observations is given in (a) and highlighted range is given in (b) with error bars to indicate the uncertainty of the data.

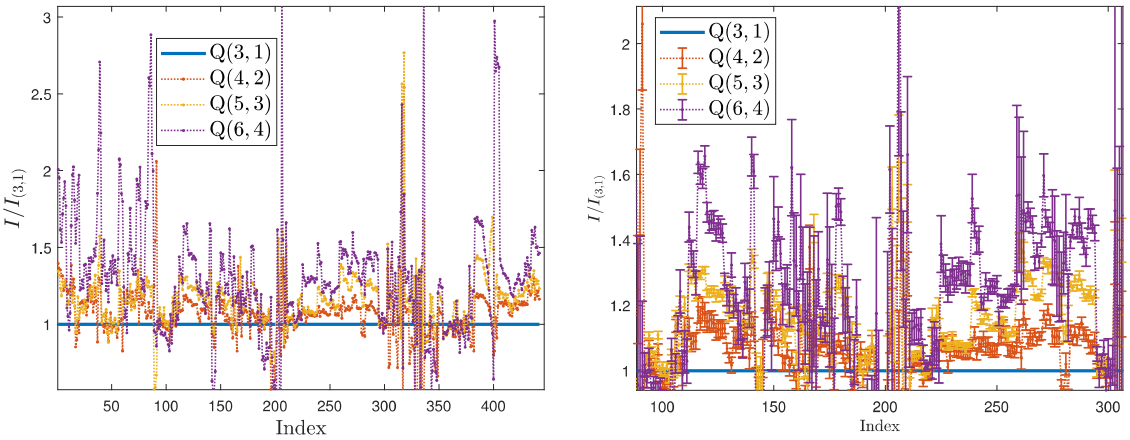

(a) (b)

Figure 5.7: Relative intensities $I_{(v',v'')}/I_{(3,1)}$ as a function of observation index. The whole data set is plotted in (a) and a selected range is plotted in (b) with error bars.

Table 5.2: Q-branch intensities relative to $\mathrm{Q}(3,1)$ calculated using a weighted mean of the full data set.

Transition	Relative intensity $[I/I_{\mathrm{Q}(3,1)}]$
$\mathrm{Q}(4,2)$	1.082 ± 0.001
$\mathrm{Q}(5,3)$	1.1399 ± 0.0001
$\mathrm{Q}(6,4)$	1.216 ± 0.002

Based on Figure 5.7, a weighted mean of the Q$(6,4)$, Q$(5,3)$ and Q$(4,2)$ intensities relative to Q$(3,1)$ was calculated with weights $w = \frac{1}{\delta I^2}$. The results are given in Table 5.2 and show that there is indeed a trend where the $(6,4)$ transition is the strongest, followed by $(5,3)$, $(4,2)$ and $(3,1)$. Similar results are reported in [24], [49] and predicted in [50], though the relative intensities in previous findings are consistently up to 20 % larger than the results presented here. The reason behind this apparent systematic error is unclear, and could in fact be attributed to latitude variations in the airglow intensity. Additionally, a nightly change in the relative intensities is found in [51] where the $(3,1)$ and $(4,2)$ transitions would be the brightest in the few hours after sunset before a turnover happens and the $(6,4)$ and $(5,3)$ become the two brightest around midnight. In conclusion, definite comparisons with literature cannot be made without extensive knowledge about sample distribution throughout the night and integration times.

K band

For the K band, a total of 735 samples in the time range from 2008 to 2016 were used to study the Q$(9,7)$ intensities in the K band. A look on the sample pool plotted versus time is given in Figure 5.8 and two example nights are shown in Figure 5.9. As in the H band,

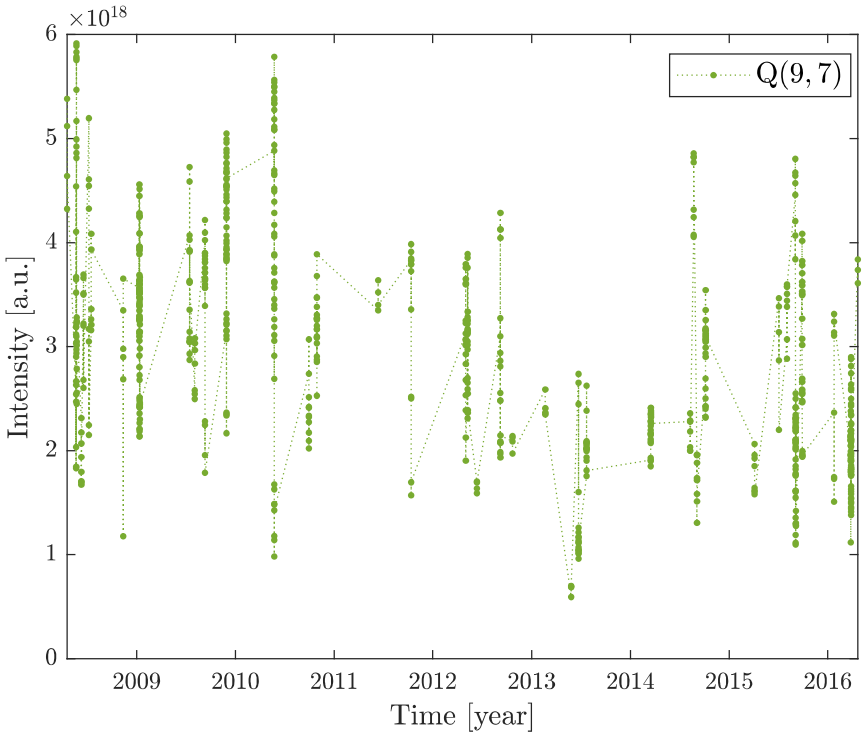

Figure 5.8: Q-branch intensities of the $(9,7)$ transitions plotted over time without error bars. The intensity is plotted in arbitrary units, but is comparable to the intensities in the H band.

it is seen that the K band data is scattered and of high variability. The intensity scale is in arbitrary units, but assumed to be comparable to the intensities in the H band. Upon first

look it is therefore possible to see that the Q$(9, 7)$ is less intense than the Q$(3, 1)$, Q$(4, 2)$, Q$(5, 3)$ and Q$(6, 4)$. As for the H band intensities, a plot of the Q$(9, 7)$ intensities as a function of index is included in Figure 5.10(a). The indices of the K band observations will not correspond to the indices of the H band observations. Figure 5.10(a) the same overall structure as seen in Figure 5.6(a). The highlighted range in Figure 5.10(a) is chosen to show the variability in intensity and uncertainty of the K filter data.

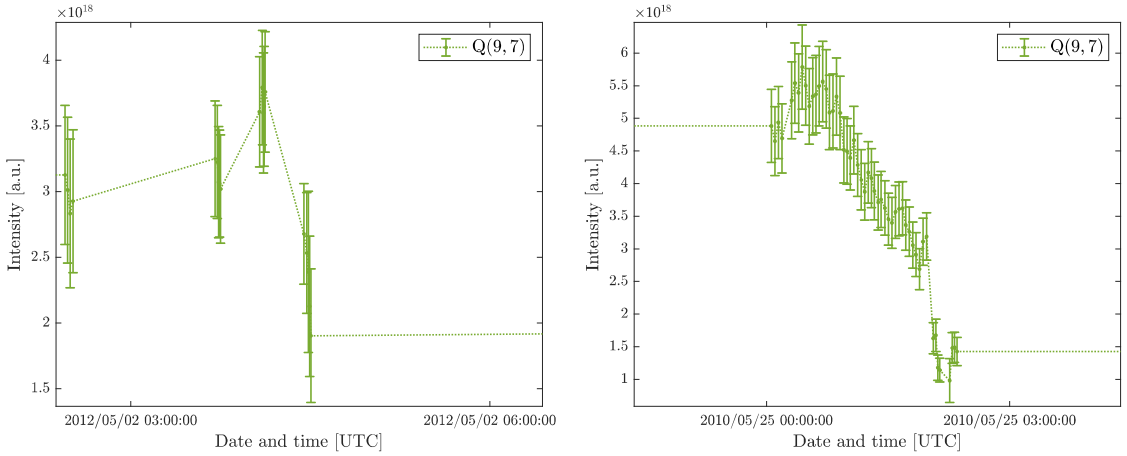

(a) (b)

Figure 5.9: Two example nights for the Q$(9, 7)$ intensity with error bars.

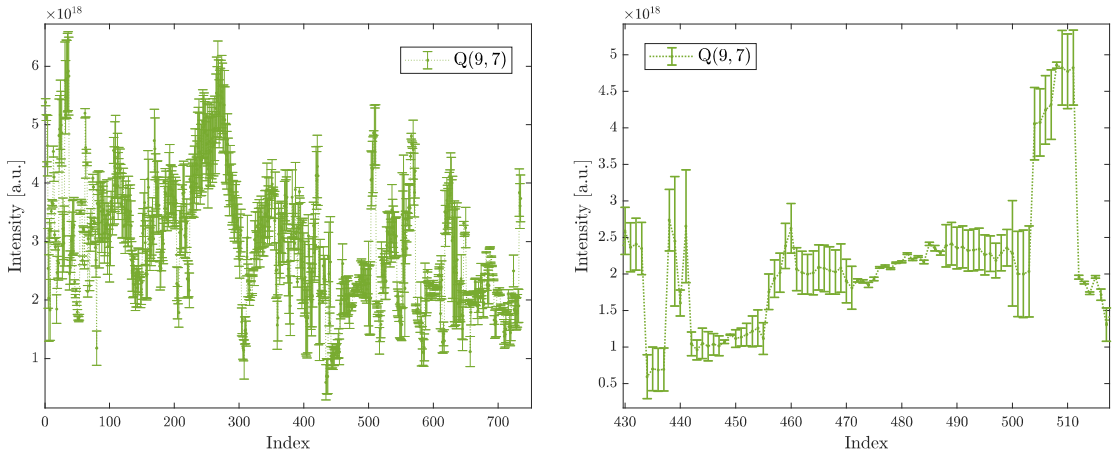

(a) (b)

Figure 5.10: Q-branch intensities of the $(9, 7)$ transition in the K band as a function of observation index. The full set of observations is given in (a) and highlighted range is given in (b) with error bars to indicate the uncertainty of the data.

Overall, the extracted Q-branch intensities from both the H band and K band appear valid and suitable for studying the nighttime cycle and seasonal cycle of the OH airglow. However, comparisons between the H band intensities relative to the K band intensities should

be made with caution due to the assumptions made related to the flat fields. Nonetheless, the shapes of the cycles can be studied with more accuracy.

5.2 Colour maps

First, the intensity development in the H and K band is visualized as colour maps, where intensity is plotted versus local solar time for each month, in Figure 5.11. This was done for the H band by adding up the $\mathrm{Q}(3,1)$, $\mathrm{Q}(4,2)$, $\mathrm{Q}(5,3)$ and $\mathrm{Q}(6,4)$ intensities, and for the K band by using the $\mathrm{Q}(9,7)$ intensity. Thus, the H band uses intensities from across the band width, creating a good basis for analysing the average intensity of the whole band. For the K band, only the $\mathrm{Q}(9,7)$ is used, resulting in a less reliable basis for interpreting the intensity of the whole band, as emission lines from the P-branch of the $(8,6)$ are also present in the band [3].

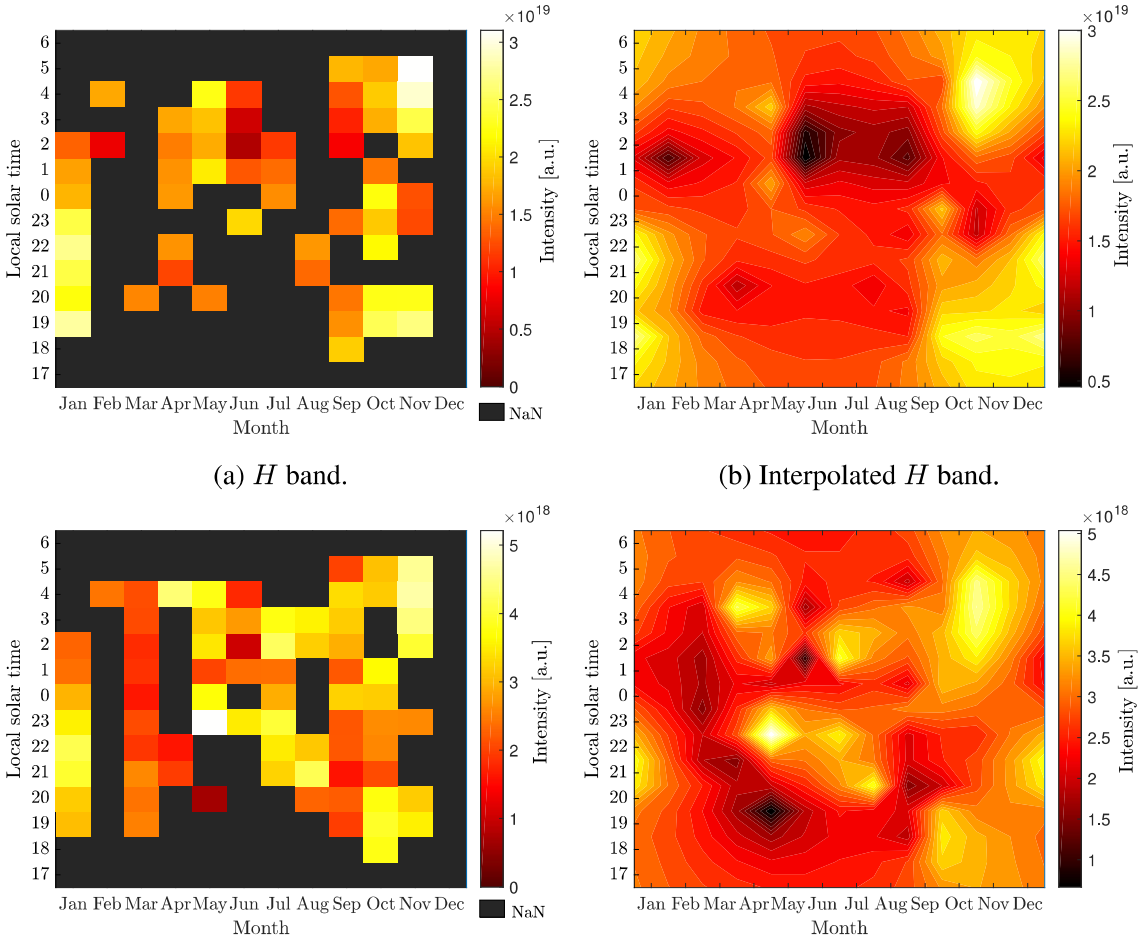

(a) H band.

(b) Interpolated H band.

(c) K band.

(d) Interpolated K band.

Figure 5.11: Colour maps showing intensity versus local solar time for each month for the H band, in (a) and (b), and K band, in (c) and (d). The plots on the left are resolved in hours on the y-axis and months on the x-axis. Areas where no observations are available are given in black. The plots on the right are interpolations based on the plots on the left.

Figure 5.11(a) and Figure 5.11(c) shows the data available in the NOTCam archive. Times where no observations are available are given in black. For the H band, February, March, April, July, August and December stands out as having observation for only a small fraction of the night, where December is missing altogether. December is also missing in the K band, and February is not well-represented.

Figure 5.11(a) and Figure 5.11(c) clearly reveal that the NOTCam data is scattered and that having more observations covering larger parts of the night could lead to significant improvements in the reliability of the results presented in this thesis. An interpolation of the data was made by repeating the data matrix three times in the x and y direction and employing an algorithm called "*Inpaint NaNs*" [52] that fills in the missing data based on the data points surrounding each NaN value. The data matrix in the center was then extracted and plotted with contour lines as shown in Figure 5.11(b) for the H band and Figure 5.11(d) for the K band. Both plots show a tendency towards a semi-diurnal intensity cycle that is more prominent during the winter than during the summer. This is consistent with the semi-diurnal tide that is present in the MLT region, which also has greater amplitude in winter than summer [53, 54, 55]. The contour plots are interpolated from sparse data and should be interpreted with caution. However, the fact that a semi-diurnal cycle is seen and is in accordance with other studies at similar latitudes suggests that intensities and trends obtained in this thesis are reliable.

5.3 Seasonal cycle

The seasonal cycle was obtained in two ways. In the first procedure, shown in Figure 5.12(a), a mean of all the intensities within a given month was used. The second method used a weighted mean of all the intensities within a given month, where $w = \frac{1}{\delta I^2}$ was used as weights. The result is shown in Figure 5.12(b). The standard error of the mean for each month is indicated by error bars in both plots.

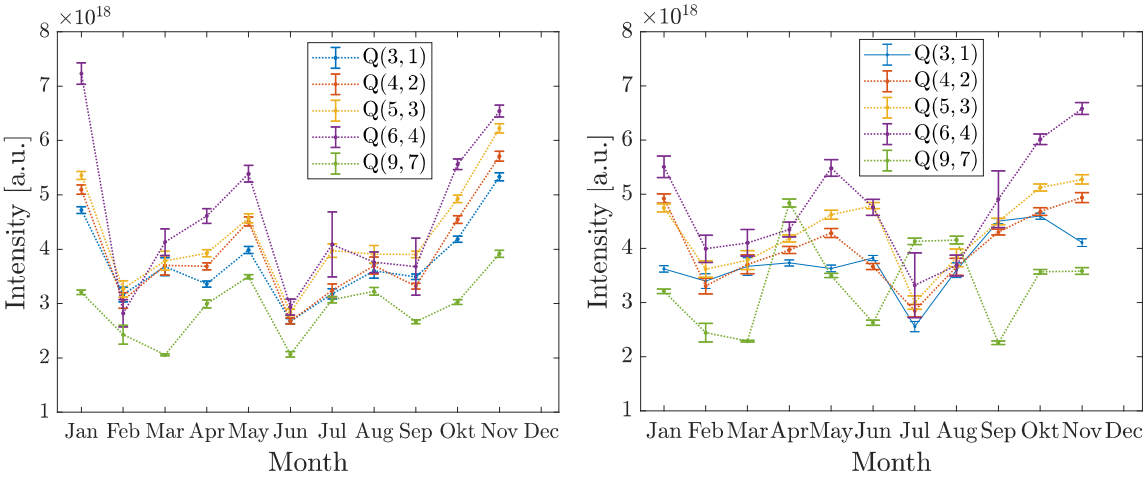

(a) Monthly mean.

(b) Monthly weighted mean.

Figure 5.12: Seasonal variation of the Q-branch intensities found using a monthly mean (a) and a monthly weighted mean (b). Data from several years are combined. The error bars represent the standard error of the mean for each month.

Data from multiple years are used for both the monthly means and weighted means. This is done because the data is too scattered within each year to compare the intensities from year to year. This is seen in Figure 5.13. By combining data from all available years there

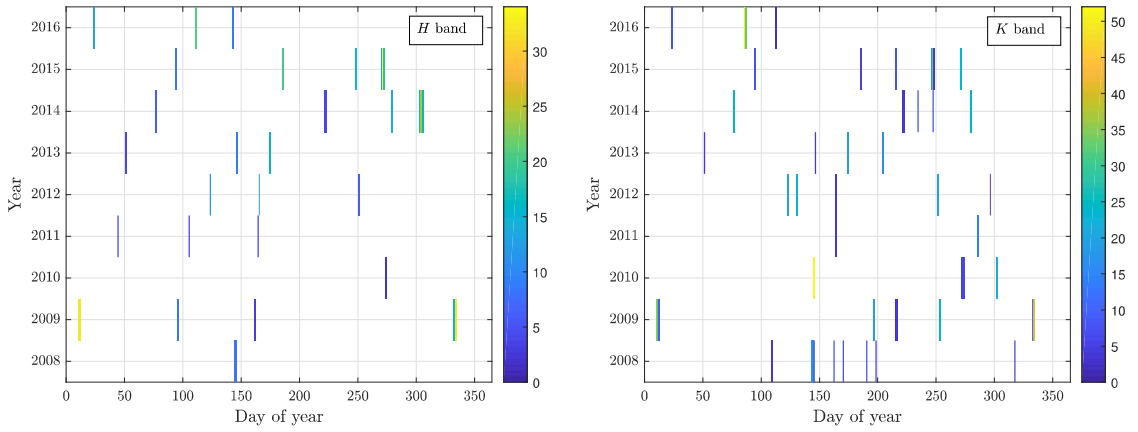

(a) H band.

(b) K band.

Figure 5.13: Distribution of observations per day of year for each year for the H band in (a) and K band in (b).

is a better foundation for calculating the average intensity for each month and produce a seasonal cycle. Figure 5.14 shows the number of observations used for each month after inter-annual combination of data. Some of the months stand out as having few measurements, namely February and December for both bands, March and August for the H band and April for the K band. It is also clear from the data distributions that some months contains measurements exclusively from certain years. As the yearly average of the airglow intensity varies with the solar cycle, this could lead to a systematic error for those months. Figure 5.13 also shows that the monthly averages could in some cases be based on just a few nights or even single nights for some months. A monthly average that is based on a just a few nights may hold more uncertainty than what is showed by the error bars. Ideally, Figure 5.13 would be filled with data points, so that each monthly average would be based on a large number of observations evenly distributed across the month, and so that seasonal cycle could be compared from year to year to study the impact of the solar cycle on the airglow layer. This cannot be done with the scattered distribution of the data available. However, if the impact of the solar cycle is small compared to the seasonal cycle of the airglow, the results presented may still be significant, at least when just the trends are interpreted rather than the absolute intensities.

Both methods produce a seasonal cycle that appears to be semi-annual, with a local maxima early-winter and early-summer and local minima late-winter and late-summer. This is in agreement with previous findings [56] where a similar cycle was found for the $(9, 3)$ transition. It is also consistent with simulations made in [57] which is discussed more in Section 5.6. A tendency towards a semi-annual cycle for $(3, 1)$ and $(4, 2)$ transitions was also found in [49]. The fact that the differences between the means and weighted means are larger than the error bounds indicate that the data set is associated with high uncertainty and variance. Some months may also be under-represented. However, the

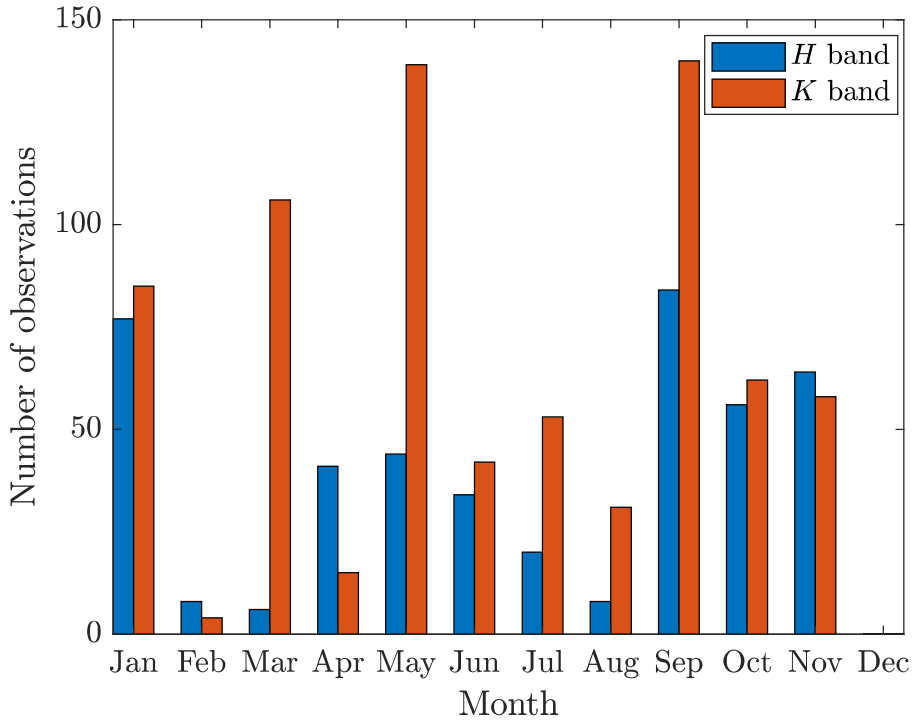

Figure 5.14: Number of observations in the H and K band for each month.

general shape is similar when using means and weighted means. A peak in the winter and a peak in the summer is present, though the Q$(9, 7)$ intensity has more sporadic ascents and descents. In the following, the seasonal cycle obtained using monthly means has been emphasized over the cycle obtained using weighted means.

5.4 Nighttime cycle

The nighttime variation of the OH layer intensity in the H and K band is plotted versus local solar time and hours past sunset in Figure 5.15. NOTCam data from all months and years are combined and binned into local solar times and hours past sunset. The mean of those bins are used to calculate the intensity, and the error bars signify the standard error of the mean. Figure 5.15(a) and Figure 5.15(c) are resolved in hours, whereas Figure 5.15(b) and Figure 5.15(d) are resolved in half-hours. The hourly averaged plots show a pattern with a maximum before midnight, a minimum shortly after midnight and an increase towards dawn. That is a semi-diurnal cycle for the airglow intensity. The half-hour resolved plots reveal more variability.

As mentioned in Section 2.2, there are mainly two effects that drive the nighttime trends in the MLT region: atmospheric tides and and photochemistry. Migrating tides follow the sun, and should thus appear as features when airglow intensity is plotted against local solar time. It is apparent from Figure 5.15(a) that a minimum takes place at 02:00 LST for the H band and 01:00 LST in the K band. Planning observations of faint as-

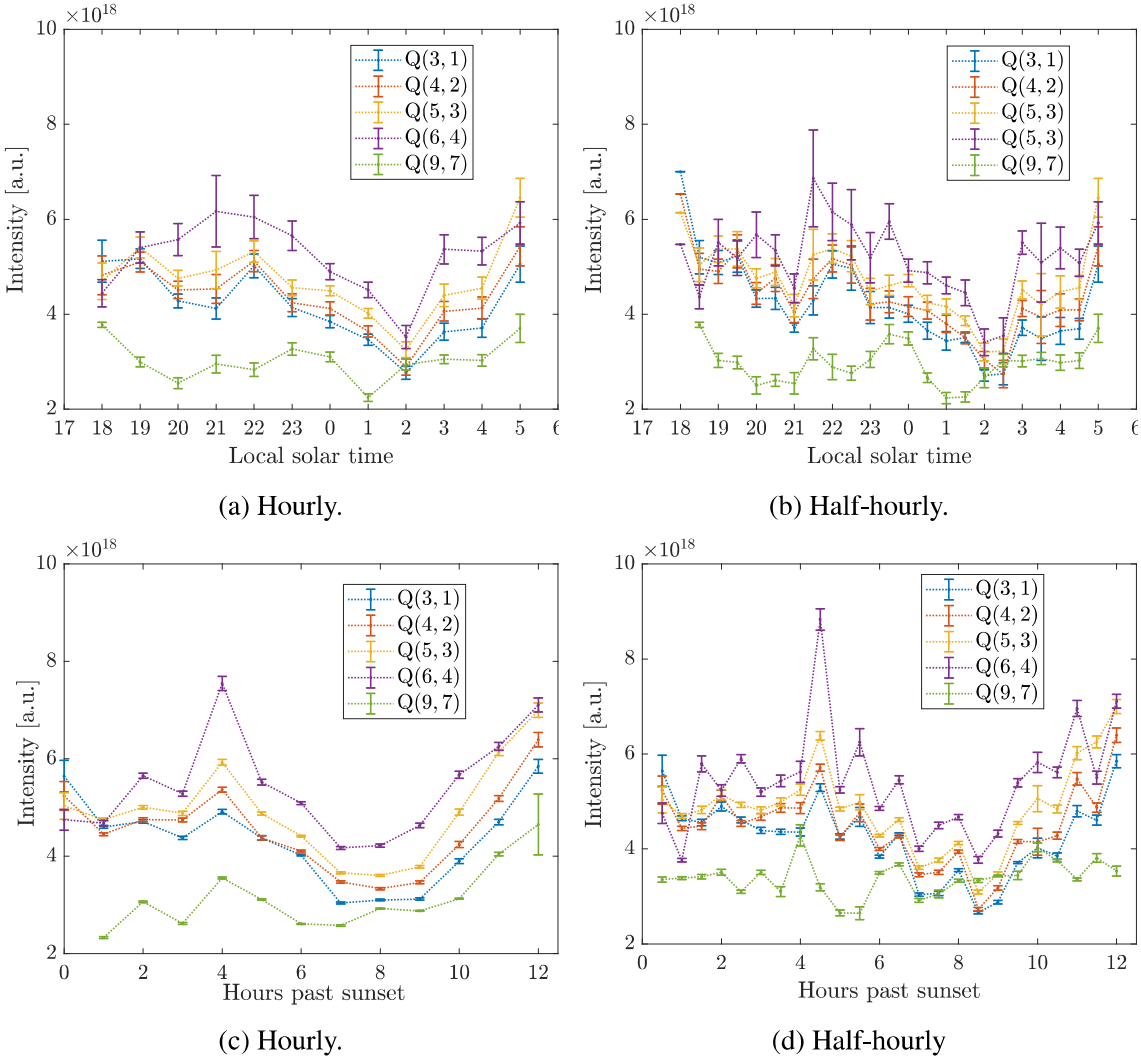

(a) Hourly.

(b) Half-hourly.

(c) Hourly.

(d) Half-hourly

Figure 5.15: Mean nighttime variation in the H and K band. The plots in (a) and (b) are intensity versus local solar resolved in hours and half-hours, respectively. (c) and (d) shows intensity versus hours past sunset resolved in hours and half-hours. The results are produced using hourly and half-hourly averages of all available data from NOTCam from 2008 to 2016, thus averaging seasonal variations in the nighttime cycle.

tronomical objects in the near-infrared at those hours may therefore be optimal for astronomers using the NOTCam. The nighttime cycle is obtained by averaging the whole year, which could be unfortunate as [56] reports a nighttime cycle that appears to change drastically dependent on season for some observatories. However, for most observatories, the nighttime cycle does not change much dependent on season, though the amplitude of the cycle appears to be smaller in the winter than in the summer. This is consistent with literature mentioned in Section 5.2.

Photochemical effects are driven by sunlight. At nighttime, the absence of the sun leads to the reactions described in Section 2.3.1 taking over and new dynamical systems taking place. Changes in the OH airglow intensity caused by these effects should depend

on time after sunset, leading to such features emerging in the hours past sunset plots in Figure 5.15(c) and Figure 5.15(d). The most prominent features seen is the peak at 4 hours past sunset, the minimum from 7 to 9 hours past sunset in H band and 6 to 7 hours past sunset in the K band, and the increase towards dawn in both bands. This increase towards dawn could be due to O and O_2 produced by sunlight leaking from the east when the day approaches.

However, as the duration of the night does not change much at the latitude of the NOT, interpreting the nighttime cycle in terms of local solar time or hours past sunset is not going to yield very different results. Therefore, it is difficult to say with certainty whether a feature is caused by photochemical or tidal effects. Such analyses are easier done at higher latitudes where the local solar time and hours past sunset are not so similar. In the following, trends are given only in terms of local solar time, as the hours past sunset results will be very similar.

5.5 Removal of seasonal cycle

A plot of the nighttime cycle is also produced after removing the seasonal cycle from each data point. This is done by repeating the monthly mean seasonal cycle in Figure 5.12(a) three times, applying a cubic spline interpolation to the five Q-branch intensities, and extracting the interpolation in the center. Subsequently, a change of variable from month m to night of year n

$$n = \frac{m}{12} \cdot 365, \tag{5.2}$$

was performed. The resulting spline interpolations are shown in Figure 5.16.

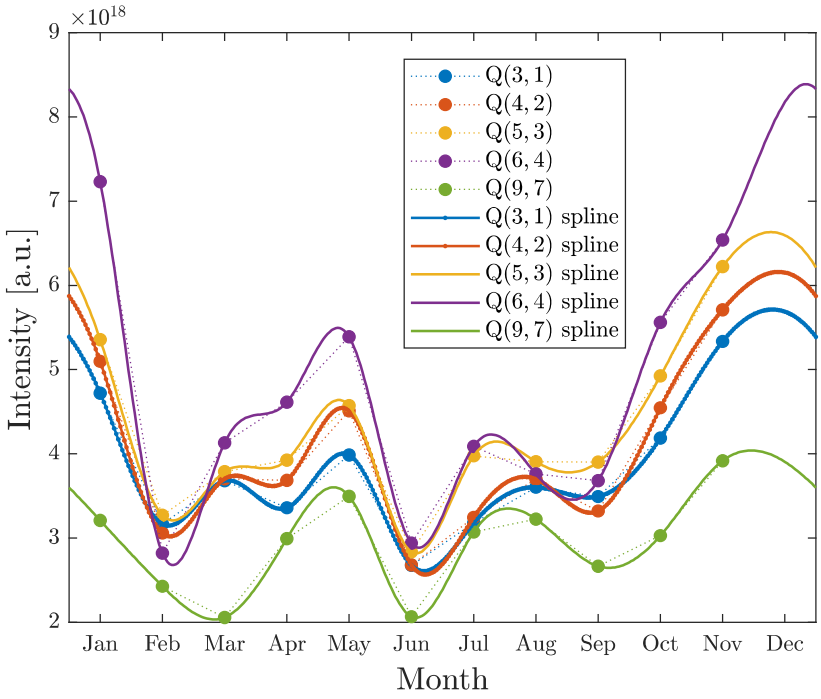

Figure 5.16: Spline interpolation used to remove the seasonal cycle from the H band and K band data.

In doing so, an average intensity as a function of the night of year of the intensity measurement was obtained for each transition. This was then subtracted from measured intensities,

$$\text{Intensity}_{\text{Season removed}} = \text{Intensity}_{\text{Original}} - \text{Intensity}_{\text{Seasonal interpolation}}, \tag{5.3}$$

and plotted in Figure 5.17. This procedure mitigates biases caused by sampling at certain nights of the year. For example, if all intensities measured at 02:00 LST where from a month where the seasonal cycle is at a minimum, that hours would be superficially low in the nightly variation plot. The procudre also highlights variations rather than static intensity differences between the transition. The y axis in Figure 5.17 shows the mean nightly intensity variation, in arbitrary units, from the mean intensity of each night. The mean monthly seasonal cycle from Figure 5.12(a) was used rather than the weighted mean in Figure 5.12(b), and the x axis is local solar time resolved in hours. The same pattern emerges for all five transition intensities, with a decrease after sunset, a local maximum between 21:00 LST and 23:00 LST, a local minimum between 01:00 LST and 02:00 LST before a rise in intensity occurs towards dawn. Some differences in the pattern from Figure 5.15(a) are seen. Mainly that the decrease after sunset is more prominent, and that the $(3, 1)$, $(4, 2)$ and $(5, 3)$ transitions show more variability around the midnight maximum. The sharp decrease in the $(6, 4)$ transition is also a new feature not seen in the previous plots. The $(9, 7)$ transition does not change much, which is an indicates that the K band observations are evenly distributed over the years and nights.

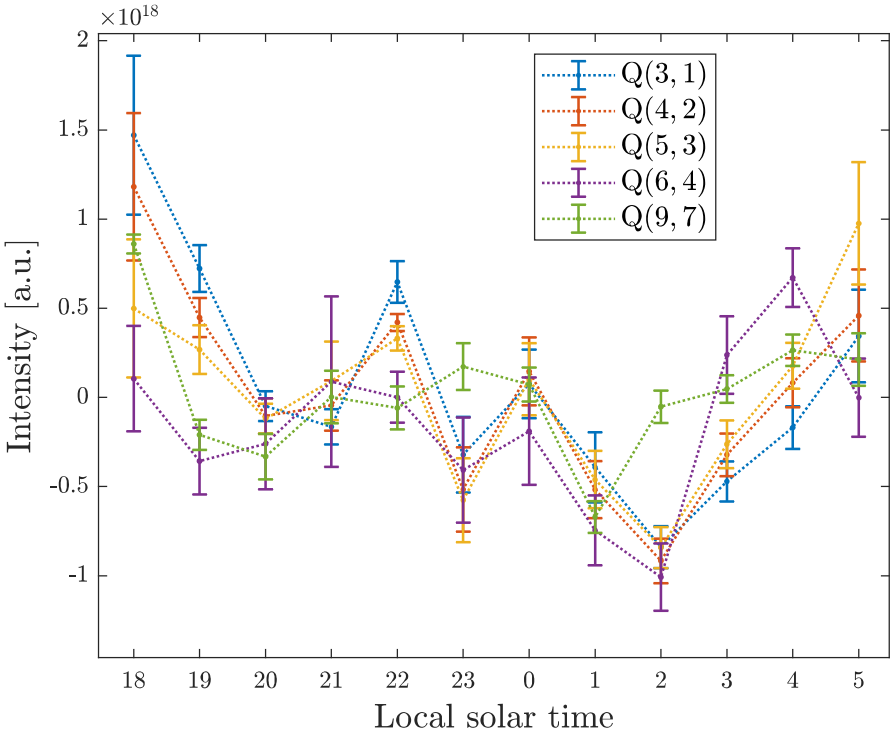

Figure 5.17: Mean nightly intensity deviation from the mean of each night as a function of local solar time. The intensity is in arbitrary units and the time axis is resolved in hours.

5.6 Removal of nighttime cycle

An adjusted plot of the seasonal cycle was produced by removing the mean nightly variation from the mean of the night in Figure 5.17 from the measured intensities. By doing this, the nighttime variability of the OH layer should be cancelled out, and any variation left in the data should be caused by seasonal effects such as long term tides and any effects summer and winter time may have on the MLT region.

A cubic spline interpolation was fitted to the different transition intensities by repeating Figure 5.17 three times, fitting the splines and extracting the center interpolations. The result is given in Figure 5.18.

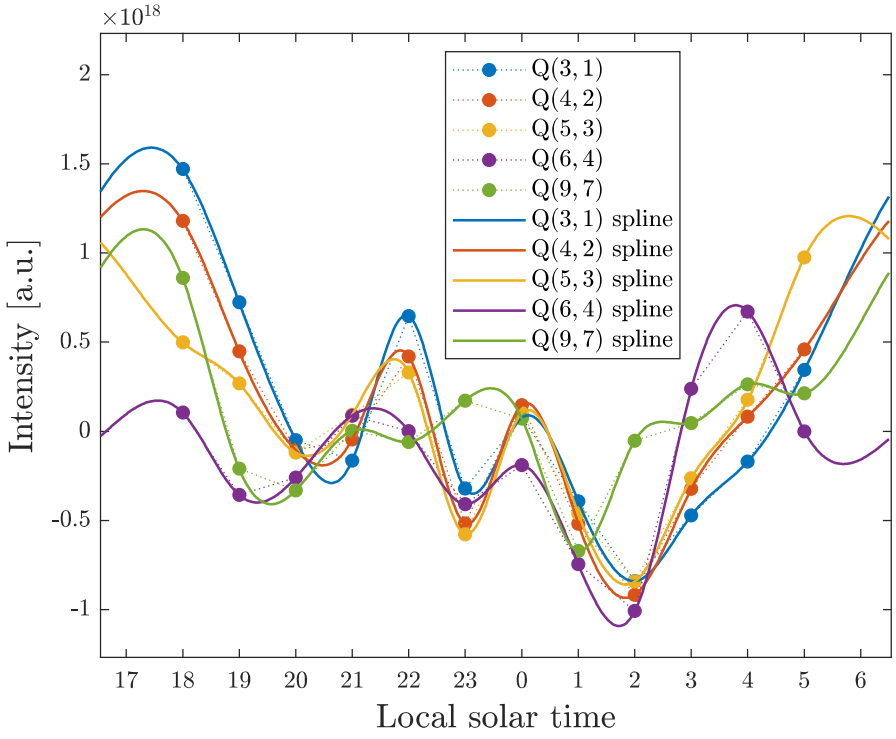

Figure 5.18: Spline interpolation used to remove the nighttime variation from the H band and K band data.

Finally, the nighttime variability was subtracted from the original intensities

$$\text{Intensity}_{\text{Night removed}} = \text{Intensity}_{\text{Original}} - \text{Intensity}_{\text{Nighttime interpolation}}. \tag{5.4}$$

The monthly means of the processed intensities was then computed and is shown in Figure 5.19. Some minor adjustments are seen, but the overall shape is remains the same as in Figure 5.12(a). This indicates that the nightly variability was already averaged out to a high degree, which could be interpreted to mean that the set of intensities available produce reliable results, despite a lack of a solid distribution of observations for all hours of every night.

The cycle depicted in Figure 5.19 is similar to the seasonal cycle simulated for the number density of OH($v' = 6$) at 31° N in [57].

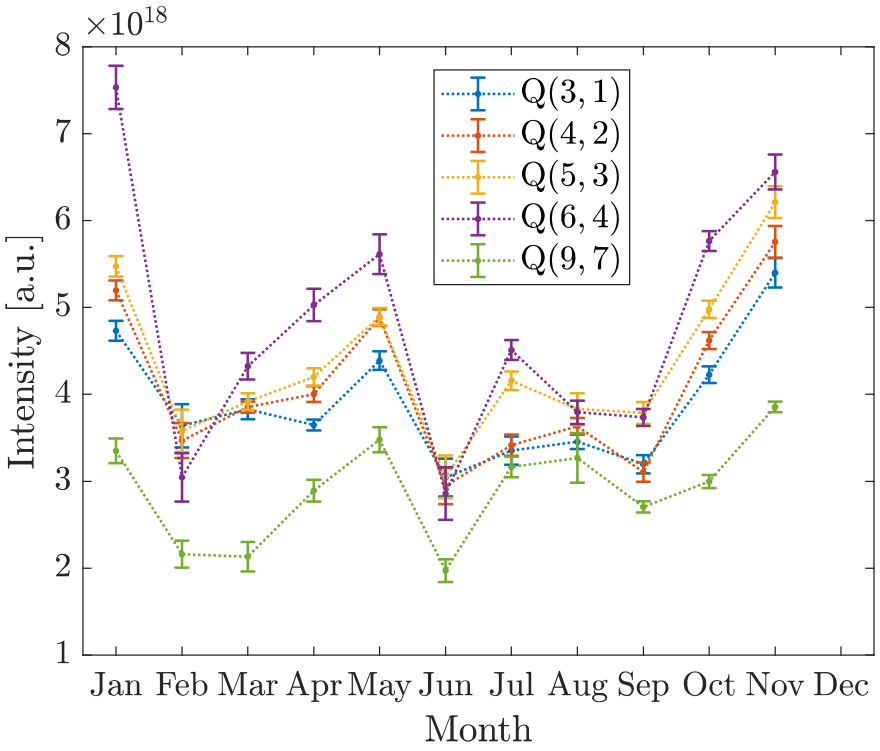

Figure 5.19: Monthly means of H and K band intensities when the nighttime variability is removed from the data. The intensity is given in arbitrary units and the error bars represent the standard error of the mean.

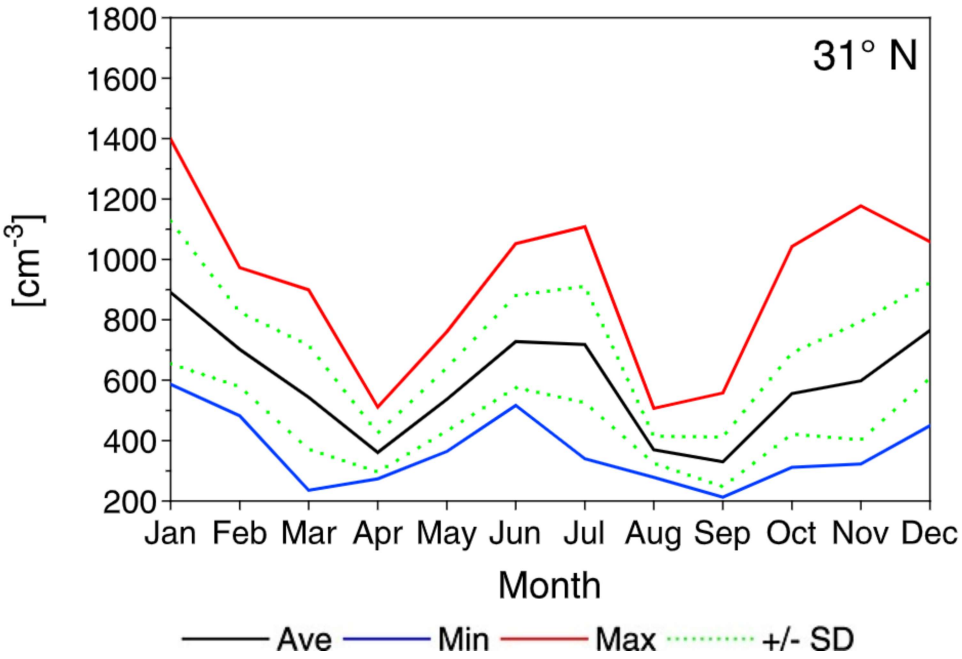

Figure 5.20: Simulated seasonal cycle of the number density of OH($v' = 6$) copied from Figure 7e in [57].

The intensity of the Q$(6, 4)$ transition should be proportional to the number density of OH$(v' = 6)$, and the population of OH$(v' = 4)$ and subsequently the intensity of the Q$(4, 2)$ should should also follow proportionally. This is in accordance with Equation (2.14) and Equation (2.18). The simulated seasonal trend is copied from its original paper and given in Figure 5.20. The simulated quantity and measured intensities have resemblances in general shape. More precisely a decrease from January to February-April, a peak in the summer, a local minimum in June-September and a rise towards the end of the year. There is some disagreement related to the exact months of maxima and minima, which is probably related to systematic errors caused by sparsity in the data distribution. The fact that Figure 5.12(a) and Figure 5.12(b) also disagrees about the months of minima and maxima supports that argument. Additionally, a perfect match is not expected to occur between a general simulation of one quantity and measurements of another, albeit related, quantity made at one geographical location. Nonetheless, the correlation between the shape of observed intensities and simulated number densities indicate that the intensities extracted from the background of the NOTCam are reliable.

5.7 Comparison with SABER data

Finally, a comparison of the seasonal cycle obtained using NOTCam data was compared to the seasonal cycle obtained using intensity measurements made by the SABER instrument mounted on the TIMED satellite. A zonal mean of latitudes from $23°45'$ N to $33°45'$ N with observations from 2008 to 2018 was used to calculate the mean monthly intensities. Two bands are available: the $1.6\,\mu m$ band and the $2.0\,\mu m$ band. The former corresponds to the H band and the latter to the K band of the NOTCam. There is not a perfect overlap between the bands of SABER and NOTCam. The $1.6\,\mu m$ band covers the $Q(4,2)$ and $Q(5,3)$ transitions, but not the $Q(3,1)$ and $Q(6,4)$. For the $2.0\,\mu m$ band, both the $Q(9,7)$ transition and the $Q(8,6)$ transition, which has not been studied in this thesis, are covered. For these reasons, it was chosen to analyse the trends from the two instruments using the $Q(4,2)$ and $Q(5,3)$ transitions as a comparison to the $1.6\,\mu m$ band, and the $Q(9,7)$ transition for comparison with the $2.0\,\mu m$ band. The four trends were normalized to their annual means, and the relative monthly deviation from the annual is plotted in Figure 5.21.

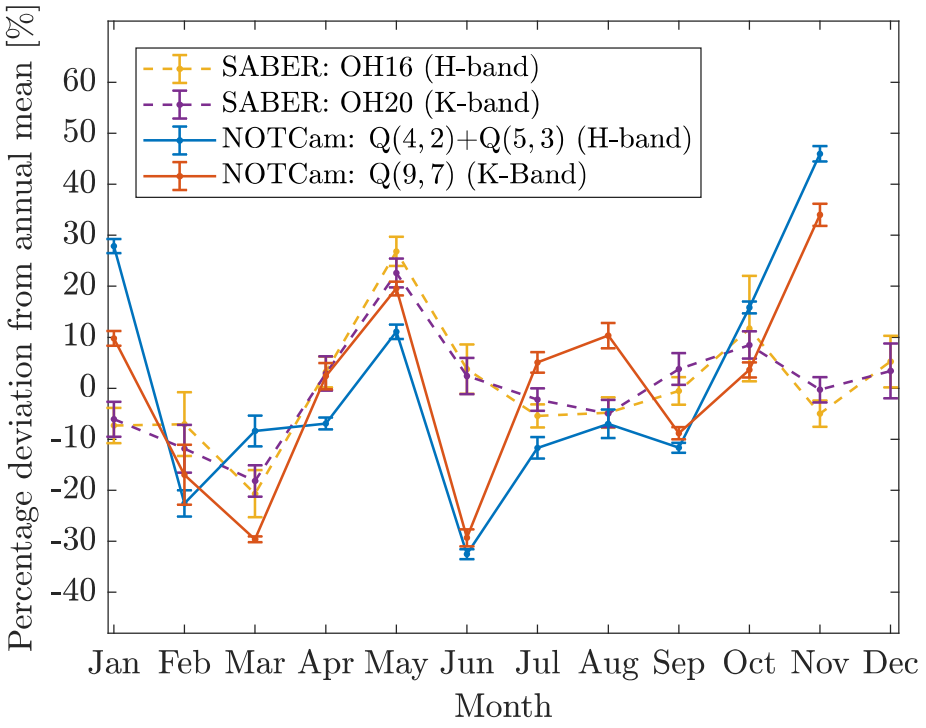

Figure 5.21: Comparison between the seasonal cycles obtained by NOTCam and SABER. The intensities are normalized to their annual means, and the relative deviation from the mean is plotted for each month. The error bars indicate the standard error of the mean for each month.

The magnitudes of deviation from annual mean is comparable for the NOTCam and SABER data. There is also strong agreement with regards to the intensity rise from March to May, with May standing out as a local intensity maximum. The minimum in June that is present the NOTCam seasonal trend is not present in the SABER trend, though there is a local

minimum in August present in the SABER data as well. The prominent rise at the end of the year, and the steep decrease after new year in the NOTCam data is not seen in the observations from SABER. The discrepancies between the seasonal cycles of the two instruments could be an indication of errors, but could also stem from the fact that the SABER cycle is based on a zonal mean with a $10°$ latitude range, whereas NOTCam is stationary. The differences could thus be local effects at the geographical location of the NOT, which are not prominent in the zonal mean.

5.8 Note on airmass

NOTCam observations taken at a telescope angle were normalized to zenith by dividing by the airmass in accordance with Equation 4.5. As previously stated, this approximation assumes a flat earth and an airglow layer of constant thickness. It is also assumed that extinction at the wavelengths studied is negligible. The normalization is thus an approximation that should decrease in accuracy for increasing airmasses. Histograms showing the distributions of observations as a function of airmass for the H and K band is given in Figure 5.22. It is seen that most observations are carried out at airmasses from 1 to 1.5,

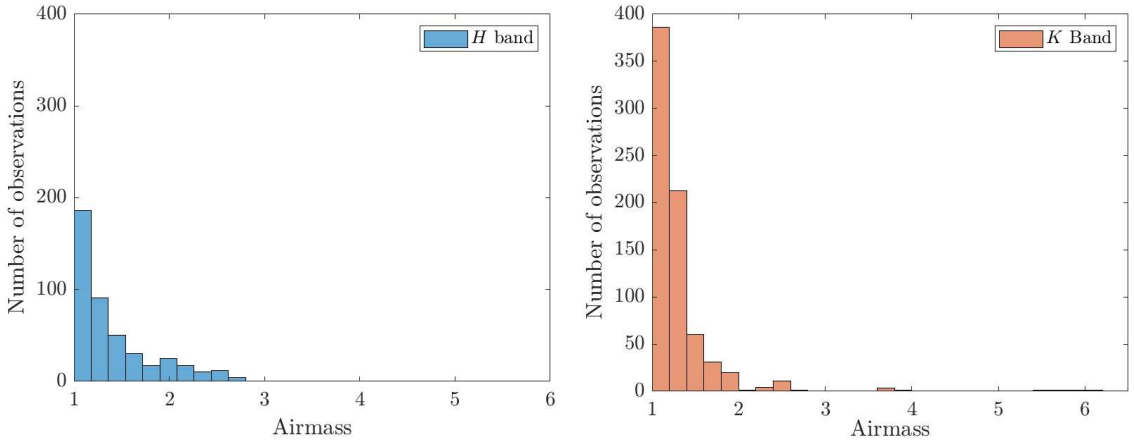

(a) H band. (b) K band.

Figure 5.22: Distribution of airmasses in the H band (a) and K band (b) used for the NOTCam data in this thesis.

though a significant amount of observations are at higher airmasses. A few observations are seen at very high airmasses up to 5 and 6. It can be argued that higher airmasses should be disregarded from the analysis, as they may introduce large systematic errors. However, there is no consensus on which airmasses to keep and which to throw away for these observations. Both the flat earth assumption and the no extinction assumption should hold for the airmasses seen in Figure 5.22, and the constant thickness assumption leads to inaccuracies independent of airmass, as the OH layer is known to fluctuate both in height and thickness [57]. Thus, it is arguably favorable to keep as many measurements as possible to average out these effects, regardless of airmass.

To check the validity of the high airmasses, the monthly means and weighted means

where calculated when only airmasses below 2 were included. The idea is that if the new monthly means differ drastically from those presented in Figure 5.12, that would be an indication that high airmasses should be disregarded from the study. Likewise, if the new monthly means do not differ noteworthy, that would be an indication that the results are valid also for high airmasses, and that it is beneficial to keep these data points in order to average out random effects from varying OH layer height and thickness. The monthly means and weighted means calculated with airmasses below 2 where matched with the corresponding monthly means and weighted means from Figure 5.12 and plotted against each other in Figure 5.23. If limiting the airmasses has no effect, the graph would show a straight line. If limiting the airmasses has an effect, data points would deviate from a straight line. A reference line $y = x$ was added to show the ideal case with no perturbation after limiting airmasses and a linear fit was performed on the data. The linear fit is very close to the reference line, and the data points do not deviate much from the line. The deviation that is seen appears random, which makes it unlikely that the high airmasses introduce a systematic error. It is concluded that including higher airmasses in the analysis does not compromise the validity of the results presented in this thesis.

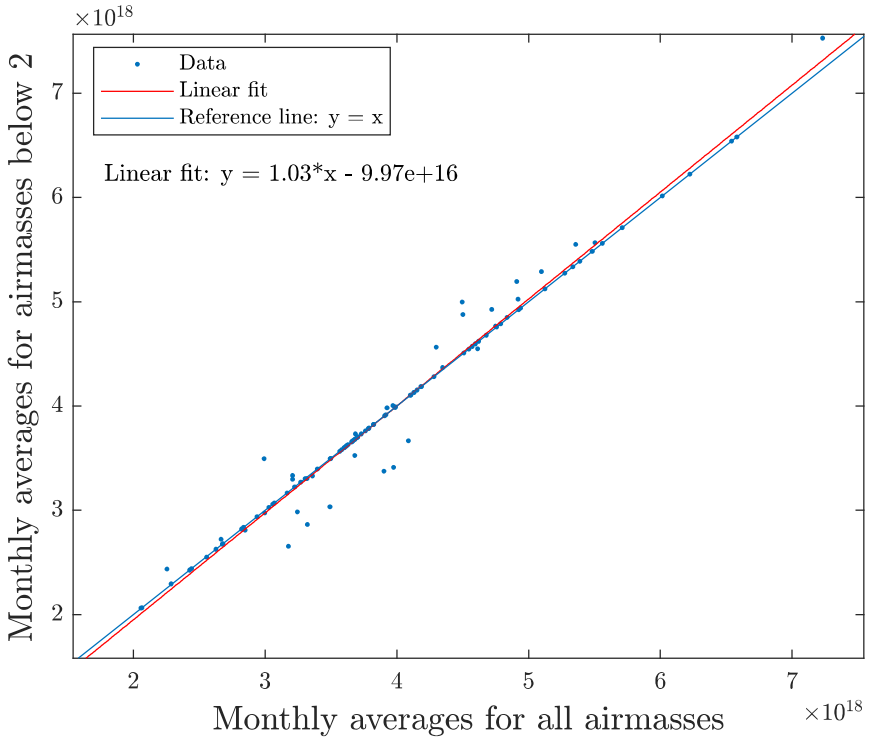

Figure 5.23: Monthly means and weighted means calculated using all data plotted against corresponding monthly means and weighted means using only airmasses below 2. The reference line shows the case where limiting the airmasses does not affect the results.

Chapter 6

Further research

This chapter discusses some of the new ideas and further work that emerge in light of the results presented in this thesis.

6.1 Absolute intensity calibration

As discussed in Section 5.1.2, the flat fields did not serve as a method for absolute calibration. However, they did serve as a way to correct for the relative spectral response of the detector. The relative variability of the different OH emissions could thus be studied in this thesis, but the absolute intensity in proper units of $\mathrm{photons\,s^{-1}\,sr^{-1}\,m^{-2}\,\mu m^{-1}}$ was not. If the absolute intensity is found, this can be compared with simulations and predictions in climate models in order to verify or improve them. From the absolute intensity, the number density and concentrations of OH(v) can also be deduced, which can also be compared with model results. If the number density of OH($v = 9$) is known, this can also be used to infer the chemical heating rates in the MLT [6]. Heating rates are integral in climate models.

Attempts at intensity calibrations could be made using standard stars of known radiance [58, 59] to simply correct the intensity obtained using solely the flat fields. Essentially, deduce the intensity of a an astronomical object using the flat field, compare with the known result and use that comparison as a correction. However, using a point source calibration to calibrate a full field of view source may not be straight forward and might need some analysis.

It could also be possible to use SABER for intensity calibration, at least to the quantities the instrument measures. If SABER data from a small geographical window confined in both longitudes and latitudes centered at the coordinates of the NOT yields a seasonal cycle that is just a factor off from the seasonal cycle found using NOTCam, this factor can be corrected. NOTCam data could then be used to infer the altitudinally integrated volume emission rate, also known as rayleigh R [60], in the $1.6\,\mu\mathrm{m}$ and $2.0\,\mu\mathrm{m}$ bands. However, SABER may not have a sufficient amount of overpasses above such a small geographical window for this to be a feasible solution.

A third possible solution is to use a precalibrated instrument, bring it to the NOT and make simultaneous measurements of the night sky. The intensities acquired by NOTCam can then be shifted to comply with the intensities obtained by the other, already calibrated, instrument. A good candidate would be the Andor spectrograph [61]. Andor can be equipped with two detector systems: an iDus InGaAs $1.7\,\mu\mathrm{m}$ detector or an iDus InGaAs $2.2\,\mu\mathrm{m}$ detector [62, 63]. The first one has a spectral range of $0.6\,\mu\mathrm{m}$ to $1.7\,\mu\mathrm{m}$, which covers the J band and $(3,1)$, $(4,2)$ and Q-branch of the $(5,3)$ transitions in the H band. It also has the advantage of being proved to work studying the $(7,4)$, $(8,5)$, $(3,1)$ and $(4,2)$ transitions, in addition to being calibrated to absolute intensity units before [64]. The second detector system has a spectral range of $0.8\,\mu\mathrm{m}$ to $2.2\,\mu\mathrm{m}$, which will cover the J band, H band and K band up to just past the Q-branch of the $(9,7)$ transition. The iDus InGaAs $2.2\,\mu\mathrm{m}$ detector can therefore be used to calibrate all three NOTCam bands simultaneously. A weakness, however, with this method, is that Andor and NOT have different fields of view. Therefore, NOT could be picking up intensities that are not resolved by Andor, effectively leading to the two instruments looking at different intensities which makes cross-calibration erroneous. This adversity could be solved by comparing average intensities over long time periods.

6.2 *J* band

NOTCam has a third filter where OH emission lines are present. This is the J filter. An analysis analogous to what has been presented in this thesis should be carried out using J filter data. The spectral range of the J filter is from $1.16\,\mu\text{m}$ to $1.33\,\mu\text{m}$, and covers the Q$(7,4)$ and Q$(8,5)$ transitions. The filter shape is plotted together with wavelengths of OH emission lines in Figure 6.1. The line strengths are given in relative populations of upper v state, which is not equivalent to intensity.

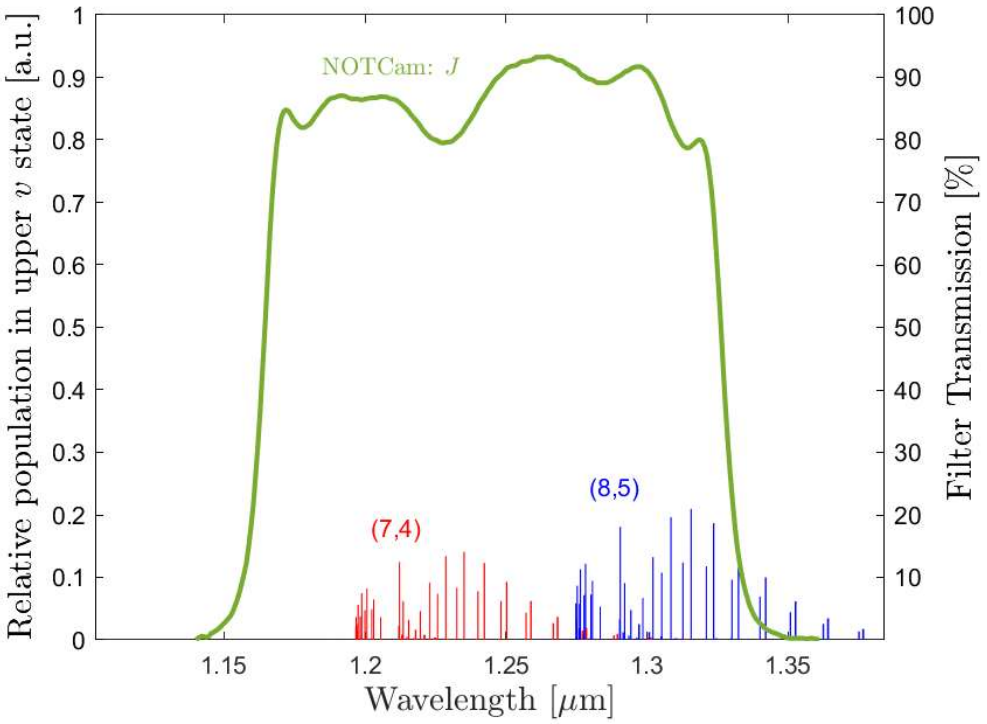

Figure 6.1: Filter shape and covered OH emission lines of the NOTCam J filter. The OH lines are plotted in relative population in upper v state, which is not equivalent to relative intensity of the two (v', v'') transitions.

A spectrum extracted from the J band using the data processing steps described in this thesis is given in Figure 6.2. The Q-branches of the $(7,4)$ and $(8,5)$ transitions are well-defined. However, it appears as if the flat area on either side of the Q-branches are smaller in J band than for the H and K band. The spectrum given in Figure 6.2 is also from an observation using a ramp-mode of $60\,\text{s}$ exposures and 10 readouts, as described in Section 3.1.2. That is a total exposure time of $600\,\text{s}$. Despite the long exposure time and high number of readouts, the noise floor looks more erratic than what is seen in for example Figure 4.8, where the H band spectra have a total exposure time of $48\,\text{s}$ and the $(9,7)$ emission is imaged with a total exposure time of $600\,\text{s}$. Combined, this could mean that extracting the Q-branch intensities may be more of a challenge in the J band, and that using images with low exposure times may not be possible. On the other hand, the J band spectrum was obtained without an available proper dark frame, but by using a master dark

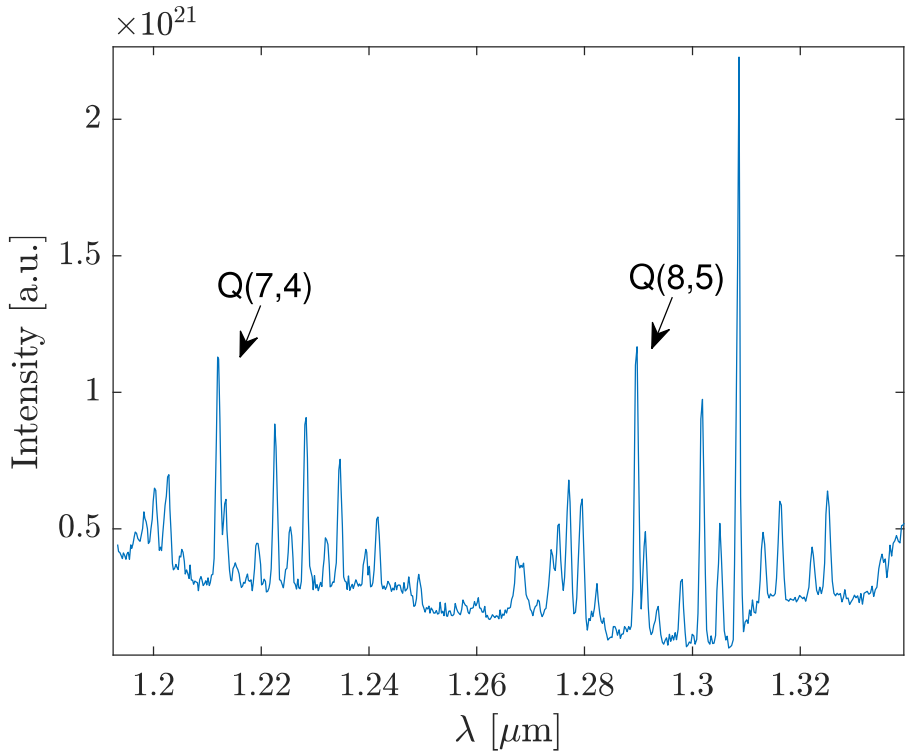

Figure 6.2: J band spectrum. The intensity is given in arbitrary units.

frame. If proper dark frames are available for other images, the signal-to-noise ratio may be improved.

A total of 452 J band images are available in the time frame from 2008 to 2016. The distribution of observation nights are given in Figure 6.3. It is comparable to that the H band distribution, and interannual combination of data to obtain a seasonal cycle of the J band intensity should therefore be possible.

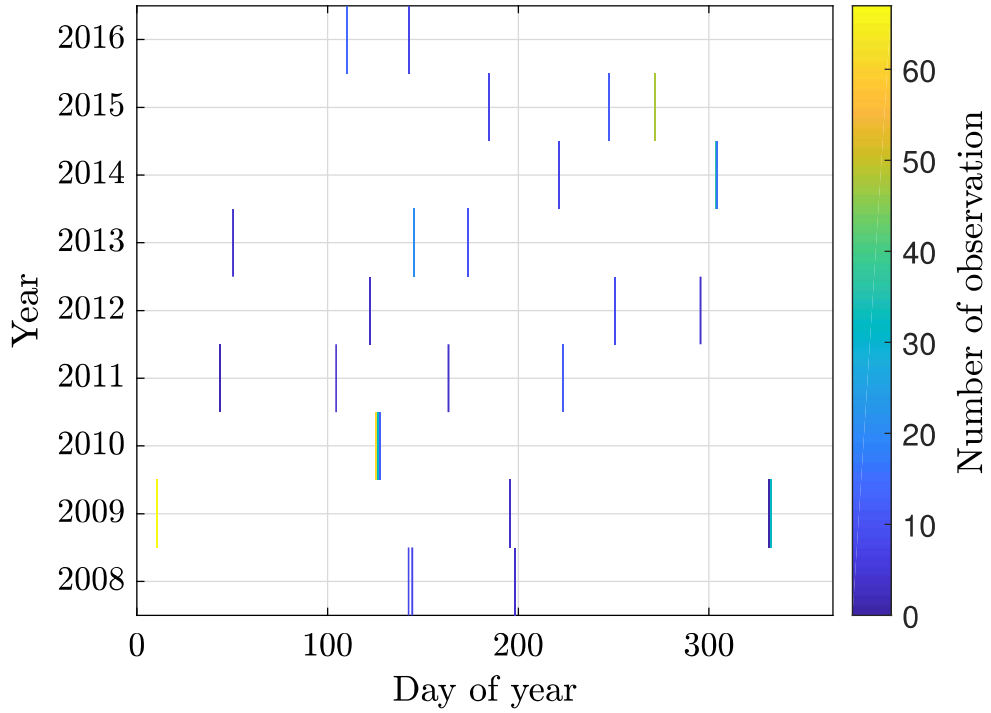

Figure 6.3: Distribution of J filter observations.

6.3 Rotational temperature trends

The rotational temperature of the OH airglow gives information about the distribution of populations in the different rotational states J for a given vibrational state v. The rotational temperatures of different v states have previously been derived using NOTCam data [44, 65]. In light of the findings of this thesis, it should be possible to implement the rotational temperature fitting presented in [44] to the coding framework developed in this thesis. Then, it will be possible to study long term trends in the rotational temperatures of the OH airglow above the NOT. Previous findings, such as [66], suggests that the time dependency of the airglow rotational temperature is correlated with the intensity. Thus, it is expected that a study of the rotational temperature trends would have the same shape as the intensity trends presented in this thesis.

6.4 Using NOTCam for atmosphere observations

Following the analysis and results of this thesis, it is clear that NOTCam can be used to study the OH airglow. The results presented here can be improved by including more observations, especially if an even and solid distribution for every day of year for multiple years was available. In that case, the seasonal cycle could be compared from year to year to increase the validity of the result. Additionally, the airglow response to the solar cycle could be studied. It would also be beneficial to have continuous observations for

whole nights. This will improve the nighttime cycle determination. Using the NOT for airglow dedicated observations will make this possible. By making sure the NOT is used for airglow observations with samples taken in the early, middle and late part of the night, for a sufficiently large amount of nights per year, where the nights are distributed over the given year, the airglow trends can be studied in greater detail and further benefit the scientific community.

Chapter 7

Conclusion

The main goal of this thesis was to develop an algorithm capable of scanning through the the NOTcam archive and extract the airglow intensities of the $(3, 1)$, $(4, 2)$, $(5, 3)$, $6, 4)$ and $(9, 7)$ Q-branches. This was achieved, and the intensities were further used to analyze the nighttime and seasonal intensity trends. The seasonal trend was also compared with the seasonal trend obtained using SABER for a zonal mean centered at the latitude of the NOT.

For the nighttime trend, a semi-diurnal cycle was found. The seasonal trend showed a semi-annual cycle. Both results are in agreement with previous findings. The coherence between the SABER and NOTCam seasonal trends serves as an indication that the extracted intensities are reliable, and a validation of the results presented in this thesis. There were some discrepancies between the SABER and NOTCam trend, but these could be attributed to local effects at the NOT that are not prominent in the zonal mean.

The main source of uncertainty is the sparse sampling distribution and the fact that both airglow trends were obtained using inter-annual combination of observations. This uncertainty can be mitigated by including more observations in the future, and using NOTCam for airglow dedicated observations. Having such observations distributed over each year, with measurements made during multiple parts of each night, will improve the results presented here and introduce the opportunity to study solar cycle effects on the airglow intensity. Another important source of uncertainty is the use of master flat fields, which can lead to a systematic error when comparing the H band intensities to the K band intensities.

In conclusion, it was found that the astronomy observations made by NOTCam can be recycled to also study the airglow intensity. Long-term trends were identified and the extracted intensities are reliable. Improvements can be made by including more data and by finding a way of calibrating the extended source intensities to absolute units.

Bibliography

[1] IPCC, *Climate Change 2013: The Physical Science Basis. Contribution of Working Group I to the Fifth Assessment Report of the Intergovernmental Panel on Climate Change*, Cambridge University Press, Cambridge, United Kingdom and New York, NY, USA, 2013, doi:10.1017/CBO9781107415324.

[2] A. B. MEINEL, *OH Emission Bands in the Spectrum of the Night Sky. I*, Astrophysical Journal, 111 (1950), doi:10.1086/145296.

[3] A. J. STEED AND D. J. BAKER, *Night sky spectral emission measurements (λ0.9–2.3 μm) using a field-widened interferometer–spectrometer*, Applied Optics, 18 (1979), doi:10.1364/AO.18.003386.

[4] A. K. SMITH, D. R. MARSH, M. G. MLYNCZAK, AND J. C. MAST, *Temporal variations of atomic oxygen in the upper mesosphere from SABER*, Journal of Geophysical Research: Atmospheres, 115 (2010), doi:10.1029/2009JD013434.

[5] M. G. MLYNCZAK, D. K. ZHOU, AND S. M. ADLER-GOLDEN, *Kinetic and spectroscopic requirements for the inference of chemical heating rates and atomic hydrogen densities from OH Meinel band measurements*, Geophysical Research Letters, 25 (1998), doi:10.1029/98GL00325.

[6] M. KAUFMANN, C. LEHMANN, L. HOFFMANN, B. FUNKE, M. LÓPEZ-PUERTAS, C. SAVIGNY, AND M. RIESE, *Chemical heating rates derived from SCIAMACHY vibrationally excited OH limb emission spectra*, Advances in Space Research, 41 (2008), doi:10.1016/j.asr.2007.07.045.

[7] R. N. GHODPAGE, M. P. HICKEY, A. K. TAORI, D. SIINGH, AND P. T. PATIL, *Response of OH airglow emissions to mesospheric gravity waves and comparisons with full-wave model simulation at a low-latitude Indian station*, Atmospheric Chemistry & Physics, 16 (2016), doi:10.5194/acp-16-5611-2016.

[8] S. WÜST, T. OFFENWANGER, C. SCHMIDT, M. BITTNER, C. JACOBI, G. STOBER, J.-H. YEE, M. G. MLYNCZAK, AND J. M. RUSSELL III, *Derivation of gravity wave intrinsic parameters and vertical wavelength using a single scanning oh(3-1) airglow*

spectrometer, Atmospheric Measurement Techniques, 11 (2018), doi:10.5194/amt-11-2937-2018.

[9] R. D. SHARMA, P. P. WINTERSTEINER, AND K. S. KALOGERAKIS, *A new mechanism for OH vibrational relaxation leading to enhanced CO_2 emissions in the nocturnal mesosphere*, Geophysical Research Letters, 42 (2015), doi:10.1002/2015GL063724.

[10] K. S. KALOGERAKIS, D. MATSIEV, R. D. SHARMA, AND P. P. WINTERSTEINER, *Resolving the mesospheric nighttime* $4.3\,\mu\mathrm{m}$ *emission puzzle: Laboratory demonstration of new mechanism for OH*(v) *relaxation*, Geophysical Research Letters, 43 (2016), doi:10.1002/2016GL069645.

[11] P. A. PANKA, A. A. KUTEPOV, K. S. KALOGERAKIS, D. JANCHES, J. M. RUSSELL, L. REZAC, A. G. FEOFILOV, M. G. MLYNCZAK, AND E. YIÄŸIT, *Resolving the mesospheric nighttime* $4.3\,\mu\mathrm{m}$ *emission puzzle: comparison of the $CO_2(\nu_3)$ and OH(ν) emission models*, Atmospheric Chemistry and Physics, 17 (2017), doi:10.5194/acp-17-9751-2017.

[12] H. L. TEXIER, S. SOLOMON, AND R. GARCIA, *Seasonal variability of the OH Meinel bands*, Planetary and Space Science, 35 (1987), doi:10.1016/0032-0633(87)90002-X.

[13] *NOTCam official webpage*. http://www.not.iac.es/instruments/notcam/. Accessed: 24.10.2018.

[14] B. Engegaard (2018), *Assessment of background data from the Nordic Optical Telescope for long-term airglow studies* (Specialization Project, TFY4510), Made available by the authour at https://bit.ly/30ZZmqS.

[15] F. LUTGENS, E. TARBUCK, AND D. TASA, *The Atmosphere: An Introduction to Meteorology*, Pearson, 12th ed., 2013.

[16] D. G. ANDREWS, *An Introduction to Atmospheric Physics*, Cambridge University Press, 2nd ed., 2010, doi:10.1017/CBO9780511800788.

[17] H. F. GOESSLING AND S. BATHIANY, *Why CO_2 cools the middle atmosphere – a consolidating model perspective*, Earth System Dynamics, 7 (2016), doi:10.5194/esd-7-697-2016.

[18] M. GARCIA-COMAS, M. JOSÉ LÓPEZ-GONZÁLEZ, F. GONZALEZ-GALINDO, J. LUIS DE LA ROSA, M. LÓPEZ-PUERTAS, M. SHEPHERD, AND G. SHEPHERD, *Mesospheric OH layer altitude at midlatitudes: Variability over the Sierra Nevada Observatory in Granada, Spain (37°N, 3°W)*, Annales Geophysicae, 35 (2017), doi:10.5194/angeo-35-1151-2017.

[19] D. SINGH AND S. GURUBARAN, *Variability of diurnal tide in the MLT region over Tirunelveli (8.7°N), India: Consistency between ground- and space-based observations*, Journal of Geophysical Research: Atmospheres, 122 (2017), doi:10.1002/2016JD025910.

[20] D. C. Fritts and M. J. Alexander, *Gravity wave dynamics and effects in the middle atmosphere*, Reviews of Geophysics, 41 (2003), doi:10.1029/2001RG000106.

[21] R. A. Vincent, *The dynamics of the mesosphere and lower thermosphere: a brief review*, Progress in Earth and Planetary Science, 2 (2015), doi:10.1186/s40645-015-0035-8.

[22] V. Y. Khomich, A. I. Semenov, and N. N. Shefov, *Airglow as an Indicator of Upper Atmospheric Structure and Dynamics*, Springer, 2008.

[23] D. R. Bates and M. Nicolet, *The photochemistry of atmospheric water vapor*, Journal of Geophysical Research, 55 (1950), doi:10.1029/JZ055i003p00301.

[24] D. Bates, *Airglow and Auroras*, Applied Atomic Collision Physics, 1 (1982), doi:10.1016/B978-0-12-478801-5.50012-8.

[25] K. S. Kalogerakis, D. Matsiev, P. C. Cosby, J. A. Dodd, S. Falcinelli, J. Hedin, A. A. Kutepov, S. Noll, P. A. Panka, C. Romanescu, and J. E. Thiebaud, *New insights for mesospheric OH: multi-quantum vibrational relaxation as a driver for non-local thermodynamic equilibrium*, Annales Geophysicae, 36 (2018), doi:10.5194/angeo-36-13-2018.

[26] H. Lefebvre-Brion and R. W. Field, *The Spectra and Dynamics of Diatomic Molecules : Revised and Enlarged Edition.*, vol. Rev. and enl. ed, Academic Press, 2004.

[27] J. M. Hollas, *Modern Spectroscopy*, Wiley, 4th ed., 2004.

[28] M. C. Abrams, S. P. Davis, M. L. P. Rao, R. Engleman, Jr., and J. W. Brault, *High-resolution Fourier transform spectroscopy of the Meinel system of OH*, Astrophysical Journal Supplement Series, 93 (1994), doi:10.1086/192058.

[29] D. D. Nelson, A. Schiffman, D. J. Nesbitt, J. J. Orlando, and J. B. Burkholder, *$H + O_3$ Fourier-transform infrared emission and laser absorption studies of $OH(X^2\Pi)$ radical: An experimental dipole moment function and state-to-state Einstein A coefficients*, The Journal of Chemical Physics, 93 (1990), doi:10.1063/1.459476.

[30] G. Herzberg, *Spectra of diatomic molecules*, vol. 1 of Molecular spectra and molecular structure, Van Nostrand, 2nd ed., 1950.

[31] A. A. Djupvik and J. Andersen, *The Nordic Optical Telescope*, in Highlights of Spanish Astrophysics V, J. M. Diego, L. J. Goicoechea, J. I. González-Serrano, and J. Gorgas, eds., Berlin, Heidelberg, 2010, Springer Berlin Heidelberg, pp. 211–218.

[32] A. Ardeberg, *Nordic Optical Telescope*, Vistas in Astronomy, 28 (1985), doi:10.1016/0083-6656(85)90076-5.

[33] J. Telting, *Spectroscopy with NOTCAM*. http://www.not.iac.es/instruments/notcam/spectroscopy/. Accessed: 20.11.2018.

[34] A. A. DJUPVIK, *New NOTCam Science Grade Array (SWIR3)*. http://www.not.iac.es/instruments/notcam/new-sci-arr.html. Accessed: 21.11.2018.

[35] A. A. DJUPVIK, *Memory effect (charge persistency)*. http://www.not.iac.es/instruments/notcam/new-sci-arr.html#memory. Accessed: 24.11.2018.

[36] T. PURSIMO, A. A. DJUPVIK, AND S. PRINS, *Description of FITS headers at the NOT*. http://www.not.iac.es/instruments/development/NOTfitsV101.pdf. Accessed: 21.11.2018.

[37] *SABER overview official webpage*. http://saber.gats-inc.com/overview.php. Accessed: 03.06.2019.

[38] M. G. MLYNCZAK, *Energetics of the mesosphere and lower thermosphere and the SABER experiment*, Advances in Space Research, 20 (1997), doi:10.1016/S0273-1177(97)00769-2.

[39] *SABER instrument official webpage*. http://saber.gats-inc.com/instrument.php. Accessed: 03.06.2019.

[40] *SABER data services official webpage*. http://saber.gats-inc.com/data_services.php. Accessed: 05.06.2019.

[41] *NetCDF official webpage*. https://www.unidata.ucar.edu/software/netcdf/. Accessed: 05.06.2019.

[42] *NOTCam official webpage: Bad pixel masks*. http://www.not.iac.es/instruments/notcam/badmask/. Accessed: 19.06.2019.

[43] C. FRANZEN, R. E. HIBBINS, P. J. ESPY, AND A. A. DJUPVIK, *Optimizing hydroxyl airglow retrievals from long-slit astronomical spectroscopic observations*, Atmospheric Measurement Techniques, 10 (2017), doi:10.5194/amt-10-3093-2017.

[44] C. Franzen (2015), *Using Background OH Airglow from astronomical Observations for atmospheric Research: A Proof of Concept* (Master's Thesis), Retrieved from http://hdl.handle.net/11250/2352123 .

[45] F. E. ROACH AND A. B. MEINEL, *The Height of the Nightglow by the Van Rhijn Method.*, The Astrophysical Journal, 122 (1955), doi:10.1086/146115.

[46] B. ENGEGAARD, *OH airglow from NOTCam*. https://github.com/BirkEngegaard/OH_airglow_from_NOTCam, 2019.

[47] S. K. RAMSAY, C. M. MOUNTAIN, AND T. R. GEBALLE, *Non-thermal emission in the atmosphere above Mauna Kea*, Monthly Notices of the Royal Astronomical Society, 259 (1992), doi:10.1093/mnras/259.4.751.

[48] T. MAIHARA, F. IWAMURO, T. YAMASHITA, D. N. B. HALL, L. L. COWIE, A. T. TOKUNAGA, AND A. PICKLES, *Observations of the OH Airglow Emission*, Publications of the Astronomical Society of the Pacific, 105 (1993), p. 940.

[49] H. Lund (2010), *Variations of the hydroxyl near infrared airglow at Rothera, Antarctica (68 °S, 68 °W)* (Master's Thesis), Available at NTNU University Library.

[50] H. S. Heaps and G. Herzberg, *Intensity distribution in the rotation-vibration spectrum of the OH molecule*, Zeitschrift für Physik A Hadrons and nuclei, 133 (1952), doi:10.1007/BF01948682.

[51] S. Noll, W. Kausch, S. Kimeswenger, S. Unterguggenberger, and A. M. Jones, *OH populations and temperatures from simultaneous spectroscopic observations of 25 bands*, Atmospheric Chemistry and Physics, 15 (2015), doi:10.5194/acp-15-3647-2015.

[52] J. D'Errico, *inpaint_nans*. https://se.mathworks.com/matlabcentral/fileexchange/4551-inpaint_nans, 2018. Accessed: 19.05.2019.

[53] M. D. Burrage, D. L. Wu, W. R. Skinner, D. A. Ortland, and P. B. Hays, *Latitude and seasonal dependence of the semidiurnal tide observed by the high-resolution doppler imager*, Journal of Geophysical Research: Atmospheres, 100 (1995), doi:10.1029/95JD00696.

[54] S. P. Zhang, C. McLandress, and G. G. Shepherd, *Satellite observations of mean winds and tides in the lower thermosphere: 2. wind imaging interferometer monthly winds for 1992 and 1993*, Journal of Geophysical Research: Atmospheres, 112 (2007), doi:10.1029/2007JD008457.

[55] M. López-González, E. Rodríguez, M. García-Comas, M. López-Puertas, I. Olivares, J. Ruiz-Bueno, M. Shepherd, G. Shepherd, and S. Sargoytchev, *Semidiurnal tidal activity of the middle atmosphere at mid-latitudes derived from O_2 atmospheric and OH(6-2) airglow SATI observations*, Journal of Atmospheric and Solar-Terrestrial Physics, 164 (2017), doi:10.1016/j.jastp.2017.08.014.

[56] R. Wiens and G. Weill, *Diurnal, annual and solar cycle variations of hydroxyl and sodium nightglow intensities in the Europe-Africa sector*, Planetary and Space Science, 21 (1973), doi:10.1016/0032-0633(73)90147-5.

[57] M. Grygalashvyly, G. R. Sonnemann, F.-J. Lübken, P. Hartogh, and U. Berger, *Hydroxyl layer: Mean state and trends at midlatitudes*, Journal of Geophysical Research (Atmospheres), 119 (2014), doi:10.1002/2014JD022094.

[58] S. K. Leggett, M. J. Currie, W. P. Varricatt, T. G. Hawarden, A. J. Adamson, J. Buckle, T. Carroll, J. K. Davies, C. J. Davis, T. H. Kerr, O. P. Kuhn, M. S. Seigar, and T. Wold, *JHK observations of faint standard stars in the Mauna Kea Observatories near-infrared photometric system*, Monthly Notices of the Royal Astronomical Society, 373 (2006), doi:10.1111/j.1365-2966.2006.11069.x.

[59] S. E. Persson, D. C. Murphy, W. Krzeminski, M. Roth, and M. J. Rieke, *A New System of Faint Near-Infrared Standard Stars*, The Astronomical Journal, 116 (1998), doi:10.1086/300607.

[60] D. HUNTEN, F. ROACH, AND J. CHAMBERLAIN, *A photometric unit for the airglow and aurora*, Journal of Atmospheric and Terrestrial Physics, 8 (1956), doi:10.1016/0021-9169(56)90111-8.

[61] *Andor official webpage*. https://andor.oxinst.com/. Accessed: 12.06.2019.

[62] *Andor official webpage: Andor iDus* $1.7\,\mu m$ *InGaAs*. https://andor.oxinst.com/products/idus-spectroscopy-cameras/idus-1-7-ingaas. Accessed: 12.06.2019.

[63] *Andor official webpage: Andor iDus* $2.2\,\mu m$ *InGaAs*. https://andor.oxinst.com/products/idus-spectroscopy-cameras/idus-2-2-ingaas. Accessed: 12.06.2019.

[64] F. T. Berge (2011), *Development of a spectrometer system to remotely sense mesospheric temperature.* (Master's Thesis), Retrieved from http://hdl.handle.net/11250/246594 .

[65] C. FRANZEN, R. E. HIBBINS, P. J. ESPY, AND A. A. DJUPVIK, *Optimizing hydroxyl airglow retrievals from long-slit astronomical spectroscopic observations*, Atmospheric Measurement Techniques, 10 (2017), doi:10.5194/amt-10-3093-2017.

[66] P. J. ESPY, J. STEGMAN, P. FORKMAN, AND D. MURTAGH, *Seasonal variation in the correlation of airglow temperature and emission rate*, Geophysical Research Letters, doi:10.1029/2007GL031034.

NTNU
Norwegian University of
Science and Technology